

# DYNQ: A Dynamic Topology-Agnostic Quantum Virtual Machine via Quality-Weighted Community Detection

Shusen Liu<sup>\*1,2</sup>, Pascal Jahan Elahi<sup>1,2</sup>, and Ugo Varetti<sup>1,2</sup>

<sup>1</sup>Pawsey Supercomputing Research Centre, Australia

<sup>2</sup>University of Western Australia, Australia

January 28, 2026

## Abstract

Quantum cloud platforms remain fundamentally non-virtualised: despite rapid hardware scaling, each user program still monopolises an entire quantum processor, preventing resource sharing, economic scalability, and quality-of-service differentiation. Existing Quantum Virtual Machine (QVM) designs attempt spatial multiplexing through topology-specific or template-based partitioning. Still, these approaches are brittle under hardware heterogeneity, calibration drift, and transient defects, precisely the conditions that dominate real quantum devices.

We present DYNQ, the first *dynamic, topology-agnostic Quantum Virtual Machine* that virtualises quantum hardware through *quality-weighted community detection*. Rather than imposing fixed geometric regions, DYNQ models a quantum processor as a weighted graph derived from live calibration data and automatically discovers execution regions that maximise internal gate quality while minimising inter-region coupling. This formulation operationalises a classical virtualisation principle, *high cohesion, low coupling*, in a quantum-native setting, yielding execution regions that are simultaneously connectivity-efficient, noise-aware, and crosstalk-resilient.

We evaluate DYNQ across five IBM Quantum backends under calibration-derived noise simulation and on two production devices, comparing against state-of-the-art QVM and standard compilation baselines. On hardware with pronounced spatial quality variance, DYNQ achieves up to **19.1% higher fidelity** and **45.1% lower output error**. Crucially, DYNQ exhibits *dead-link immunity*: when transient hardware defects cause baseline executions to fail completely, DYNQ dynamically becomes increasingly heterogeneous, achieving over **86% fidelity**. Under multi-tenant execution, fidelity remains statistically stable ( $r = -0.012$ ) as concurrency scales from 2 to 18 programs, enabling up to **90% reduction in job cost** through safe batching.

By transforming calibrated device graphs into adaptive virtual hardware abstractions, DYNQ decouples quantum programs from fragile physical layouts and enables reliable, high-utilisation quantum cloud services. As quantum processors scale toward thousands of qubits and become increasingly heterogeneous, DYNQ establishes a principled foundation for topology-independent, quality-aware quantum virtualisation.

## 1 Introduction

The classical cloud computing revolution was built on virtualisation, namely the ability to partition physical servers into isolated virtual machines serving multiple tenants simultaneously. This fundamental abstraction transformed the economics of computing, enabling resource sharing, workload isolation, and differentiated quality of service (QoS). Despite its rapid growth, quantum cloud computing lacks this foundational capability. Platforms such as IBM Quantum [12], Amazon Braket [1], and Google Quantum AI [11] support users through a primitive sequential execution model: each program monopolises an entire quantum processor, regardless of size, precluding the multi-tenant resource sharing that defines modern cloud services.

This limitation becomes increasingly costly as quantum processors scale. IBM’s Heron r2 with 156 qubits and Heron r1 with 133 qubits processors [13] routinely execute 5-qubit algorithms, leaving over 97% of the hardware idle. With processors projected to reach thousands of qubits, this inefficiency will worsen dramatically. More critically, the sequential execution model prevents the economic scaling that classical clouds achieve through resource sharing; quantum cloud providers cannot amortise the cost of expensive hardware across concurrent users. Furthermore,

---

<sup>\*</sup>Corresponding author: shusen.liu@csiro.au

on large devices, such sparse compilations exacerbate a well-known compiler pathology: conventional routing and layout heuristics operate on a huge coupling graph and are therefore prone to becoming trapped in poor local optima. The concept of *Quantum Virtual Machines* (QVMs) aims to bridge this gap by virtualising quantum resources, enabling isolation, sharing, and scalable utilisation of quantum processors. Broadly, existing QVM efforts fall into two conceptual categories. *Hardware-level QVMs* partition a single quantum processor into multiple isolated execution regions to support multi-tenant concurrency, while *program-level QVMs* virtualise execution through circuit fragmentation, gate virtualisation, or post-processing to extend the effective scale of computation beyond native hardware limits. Although these approaches address different bottlenecks, they share a common goal: decoupling logical quantum workloads from rigid physical hardware constraints.

Despite rapid progress in quantum hardware and cloud access models, existing quantum virtual machine (QVM) designs still fall short of providing a robust, general-purpose abstraction for heterogeneous quantum clouds. Current approaches essentially treat virtualisation as a static mapping problem [38, 40], binding virtual machines to fixed topological assumptions, nominal calibration snapshots, or coarse isolation boundaries. While such designs can be effective in controlled settings, they struggle to scale as devices grow larger, architectures diversify, and hardware behaviour becomes increasingly non-stationary.

At scale, these limitations have systemic consequences. Topology-bound virtualisation inhibits portability across processor generations, forcing repeated redesign as coupling structures evolve. Static region definitions become brittle due to calibration drift and transient defects, leading to sudden allocation failures or forcing execution through degraded hardware paths. Meanwhile, quality-agnostic abstractions obscure large spatial variations in gate fidelity and crosstalk, preventing cloud providers from offering differentiated quality of service or from systematically suppressing inter-tenant interference as concurrency increases. Together, these factors undermine both the performance and the economic viability of quantum cloud platforms, where efficient resource sharing and predictable execution quality are essential.

These observations suggest that the limitations of existing QVMs are not merely engineering artefacts, but symptoms of a deeper abstraction gap: current designs do not treat the calibrated device graph itself as a dynamic, quality-structured runtime resource. Addressing this gap requires rethinking QVMs as algorithmically derived, calibration-aware virtual devices that evolve with hardware conditions rather than encoding fixed assumptions about topology, stability, or uniformity. We elaborate on these limitations and position prior work in Section 2.7.

**Our approach.** We present DYNQ, a *Dynamic Topology-Agnostic QVM* that fundamentally reimagines quantum resource virtualisation. Rather than imposing external geometric patterns, DYNQ discovers natural QVM boundaries through quality-weighted community detection. The key insight draws from classical virtualisation: effective resource isolation requires **high internal cohesion** (strong connectivity within regions) and **low external coupling** (weak connections between regions). In quantum hardware, this translates to grouping qubits connected by high-fidelity gates while placing boundaries along noisy, crosstalk-prone couplers.

In principle, DYNQ models the processor as a weighted graph in which edge weights encode gate fidelities, and applies the Louvain algorithm [5], a modularity-maximising community detector, to discover hardware regions with high internal quality and low boundary crosstalk. This approach requires zero topology-specific configuration: the same algorithm discovers suitable regions on IBM’s heavy-hex [16], Rigetti’s square-lattice [32], and IQM’s star-connected architectures [31]. Dynamic re-discovery adapts to transient defects by regenerating regions from current calibration data.

The community detection formulation directly addresses the crosstalk-isolation challenge inherent in multi-tenant execution. In quantum hardware, couplers with low gate fidelity often exhibit elevated crosstalk, arising from frequency proximity, parasitic interactions, or strong residual coupling. By assigning lower weights to such edges, the modularity objective naturally places region boundaries along these low-quality couplers, separating tenants across the most interference-prone links. This results in implicit buffer zones that suppress cross-region error propagation without reserving dedicated idle qubits. Our experiments validate this formulation-driven isolation effect. As the number of concurrent tenants increases from 2 to 18, circuit fidelity remains statistically stable ( $r = -0.012$ ), indicating that inter-tenant interference does not accumulate with load. This stability confirms that quality-weighted community boundaries provide robust crosstalk suppression under realistic multi-tenant concurrency.

**Contributions.** This paper makes the following methodological and empirical contributions:

- **Dynamic Topology-Agnostic QVM Architecture.** We introduce an approach to quantum virtualisation that discovers QVM regions through quality-weighted community detection. The algorithm operates on any coupling graph without modification, handling transient defects through dynamic re-discovery.
- **High-Cohesion/Low-Coupling Partitioning Methodology.** We formalise quantum resource partitioning as modularity optimisation, where the objective function tends to produce regions with strong internal connectivity (supporting efficient circuit compilation) and weak external coupling. This principled formulation connects

quantum virtualisation to established graph algorithms.

- **Fault Recovery Capability.** We demonstrate that DYNQ recovers program execution with over 86% fidelity proxy when standard compilation produces complete failures (0% fidelity proxy) due to transient hardware defects. This qualitative capability has implications for the reliability of quantum cloud systems.
- **Comprehensive Multi-Backend Evaluation.** We conduct extensive experiments across five simulated IBM backends and two real quantum devices, comparing against standard Qiskit compilation as a baseline. On high-variance hardware, DYNQ reduces the total variation distance to the ideal output distribution by 45.1%, corresponding to a 19.1% improvement in result fidelity. Batch scalability experiments further demonstrate stable multi-tenant performance under increasing concurrency, enabling substantial cost reduction through job batching.

## 2 Background

We provide background on the classical virtualisation principles that inspire our approach, quantum processor architectures across vendors, the noise challenges specific to multi-tenant execution, and limitations of existing QVM approaches.

### 2.1 From Classical to Quantum Virtual Machines

Classical virtual machines (VMs) revolutionised computing infrastructure by enabling multiple isolated execution environments on shared physical hardware. The key principles underlying classical VM success translate directly to quantum virtualisation:

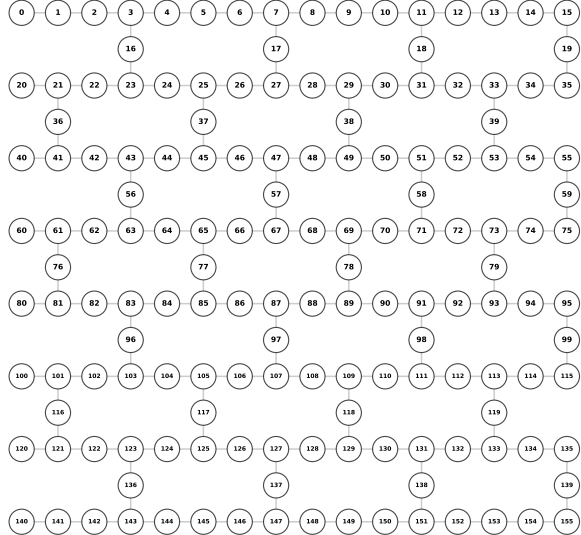
**Resource partitioning.** Physical resources (CPU cores, memory, storage) are divided into isolated pools assigned to different tenants. Each VM sees a virtualised view of hardware resources, unaware of other tenants. In quantum systems, this corresponds to partitioning qubits and couplers into disjoint regions, each of which presents an independent virtual quantum processor to its assigned program.

**Strong isolation.** Classical hypervisors enforce isolation between virtual machines through hardware-supported memory protection (e.g. Memory Protection Keys [28], Capability Hardware Enhanced RISC Instructions [42], Memory Integrity Enforcement [3]), privilege separation [6], and controlled resource multiplexing [35]. As a result, interference between VMs, whether arising from resource contention or information leakage, is prevented or strictly bounded by design.

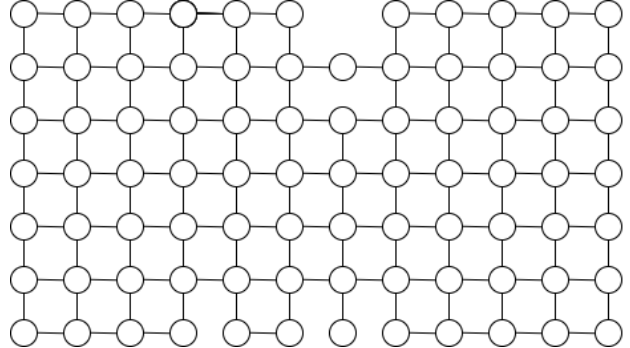
Quantum isolation is fundamentally more challenging. Beyond classical-style resource contention, quantum systems admit intrinsic non-classical correlations: quantum states may become entangled, either intentionally through algorithmic operations or unintentionally through residual coupling, crosstalk, or imperfect control, even when programs do not share qubits. Such correlations cannot be fully eliminated by logical separation alone, and once established, their effects propagate coherently across the hardware substrate [24]. Consequently, effective quantum virtualisation requires isolation boundaries explicitly aligned with the underlying hardware physics to attenuate both classical interference channels and unintended quantum correlations across regions.

**Quality-of-service differentiation.** Classical cloud providers offer tiered service levels such as on-demand, reserved, and spot instances in AWS [2], which offer different performance and pricing trade-offs, and Standard vs. Premium network service tiers in Google Cloud Platform [10], with differentiated performance guarantees. Quantum QoS differentiation requires analogous quality stratification: identifying high-fidelity regions for premium tenants and lower-quality regions for best-effort workloads. Unlike classical workloads, some quantum applications, such as variational quantum algorithms (e.g., Variational Quantum Algorithms, VQAs), exhibit tolerance to noise and can operate effectively on moderate-quality regions, whereas other algorithms are far more sensitive to error rates and require high-fidelity execution to produce useful results.

**Dynamic adaptation.** Modern hypervisors and orchestration systems such as Kubernetes support a variety of dynamic resource management capabilities, including live migration of virtual machines, horizontal and vertical auto-scaling of workloads, and automatic fault recovery in response to hardware failures or load changes. For example, Kubernetes can automatically adjust the number of running pod replicas based on demand and reschedule failed workloads to maintain availability and performance [39]. Quantum systems exhibit even more severe dynamic behaviour. In addition to transient defects that can disable qubits or couplers between calibration cycles, qubit parameters such as coherence times and gate fidelities drift over time due to environmental fluctuations and calibration adjustments. These effects make static region definitions brittle: a configuration that is valid immediately after calibration can become suboptimal or invalid after the next calibration update. Effective QVMs must therefore continually adapt region boundaries and allocations in response to evolving calibration data rather than relying on fixed, static configurations.



(a) IBM Heron r3 series



(b) Rigetti Ankaa-3

Figure 1: **Representative coupling maps of superconducting quantum processors.** Each node denotes a physical qubit, while edges indicate pairs of qubits supporting native two-qubit gates. The illustrated coupling graphs highlight the structural diversity and sparsity of contemporary superconducting hardware. (a) IBM Heron r3 series adopts a heavy-hex-inspired lattice with deliberately reduced connectivity to mitigate frequency collisions and crosstalk. (b) Rigetti Ankaa-3 follows a lattice-based layout with localised connectivity constraints. Despite differing geometric organisations, both architectures exhibit irregular and non-uniform coupling patterns, posing significant challenges for topology-aware quantum compilation and motivating the need for hardware-agnostic allocation and mapping strategies.

The related theoretical foundations of quantum programming and resource management have been established in prior work. Ying’s foundational treatment [43] develops formal semantics for quantum programs, providing a rigorous basis for reasoning about quantum resource allocation. Recent work on quantum resource theories [7] characterises quantum resources in terms of their inter-convertibility under allowed operations, though practical QVM systems must also address the physical constraints of real hardware.

## 2.2 Quantum Processor Architecture

A superconducting quantum processor is composed of physical qubits, most commonly implemented as transmon qubits, which are nonlinear superconducting circuits designed to reduce sensitivity to charge noise. Each qubit interacts with others through engineered couplers such as resonators or capacitive connections, and the set of supported two-qubit interactions is described by the processor’s *coupling map*. Unlike classical processors with uniform interconnects, superconducting qubit coupling maps are inherently sparse and irregular due to constraints on physical layout and the need to avoid unwanted interactions and frequency crowding between neighbouring qubits. Limited connectivity is a deliberate design choice that enables individual qubit control and high-fidelity operations, but it also means that gates between non-adjacent qubits must be realised through sequences of SWAP operations or other routing primitives. Such routing incurs additional overhead and increases effective error rates as circuits grow in size and depth [44].

As illustrated by the representative coupling maps in Fig. 1, each physical qubit in a superconducting processor is associated with heterogeneous quality metrics obtained through periodic calibration, typically performed daily or after thermal cycles. Among these, the coherence times  $T_1$  (energy relaxation) and  $T_2$  (dephasing) quantify how long quantum information can be reliably preserved. On current superconducting platforms, these coherence times are typically on the order of 100–500  $\mu$ s for IBM devices, 10–50  $\mu$ s for Rigetti hardware [32], and comparable ranges for contemporary IQM systems.

These coherence limits impose a hard upper bound on the effective circuit depth: all gate operations must be completed before quantum states decohere. In addition, single-qubit gate error rates, typically ranging from  $10^{-4}$

to  $10^{-3}$ , capture the probability of faulty unitary operations arising from imperfectly calibrated microwave pulses. Readout errors, generally in the range of  $10^{-3}$  to  $10^{-2}$ , further contribute to overall execution infidelity due to imperfect discrimination between the  $|0\rangle$  and  $|1\rangle$  measurement outcomes.

Taken together with the sparse and irregular coupling structures shown in Fig. 1, these non-uniform and time-varying hardware characteristics significantly complicate quantum circuit compilation and motivate the need for allocation and mapping strategies that jointly account for topology and qubit quality.

Two-qubit gates are the dominant source of error in near-term quantum computation, as they require precise coordination between qubits and are inherently more sensitive to control noise, residual coupling, and calibration imperfections than single-qubit operations. For most superconducting platforms, the error rates of native two-qubit gates are typically an order of magnitude higher than those of single-qubit gates, commonly ranging from  $10^{-3}$  to  $10^{-2}$ . Although the physical realisation of two-qubit gates varies across hardware platforms, their performance is consistently governed by local device parameters. On superconducting processors, two-qubit gate fidelity depends on factors such as qubit frequency detuning, effective coupling strength, crosstalk from nearby control lines, and sensitivity to environmental noise. These parameters are shaped by fabrication variability and the local electromagnetic environment, leading to pronounced spatial heterogeneity in gate quality across the chip. Different quantum processors instantiate two-qubit interactions using distinct mechanisms. For example, IBM devices employ the echo cross-resonance (ECR) gate, which is realised by driving one qubit at the transition frequency of its coupled neighbour. Other platforms, such as fixed-frequency transmon architectures with tunable couplers or alternative interaction schemes, exhibit analogous sensitivity to local frequency alignment and coupling conditions. Despite these architectural differences, spatially correlated variations in two-qubit gate errors are a common feature across superconducting quantum processors.

This effect is clearly visible in our experimental data. On a 156-qubit processor, measured two-qubit gate error rates range from approximately 0.3% to over 3%, with errors exhibiting strong spatial clustering into high-quality and low-quality regions rather than being uniformly distributed.

### 2.3 Quantum Processor Topologies

Different quantum hardware vendors have adopted distinct connectivity topologies, each with implications for virtualisation. Understanding these differences is essential for designing topology-agnostic QVM systems.

**IBM Heavy-Hex Topology.** IBM’s Eagle (127 qubits), Heron (133 qubits and 156 qubits), and Condor (1121 qubits) processor families employ the heavy-hex topology [13], a sparse superconducting coupling graph designed to support surface code and other nearest-neighbour quantum error correction schemes. In this layout, qubits are arranged in an augmented hexagonal pattern with additional “bridge” qubits that connect neighbouring hexagons. The resulting structure ensures that no qubit has more than three two-qubit neighbours, yielding an average degree of approximately three for a processor with  $n$  qubits.

This constrained connectivity arises from the need to balance planar nearest-neighbour interactions with the avoidance of frequency collisions and excessive crosstalk. Compared to an idealised rectangular grid with degree four connectivity, heavy-hex imposes irregular neighbourhoods and missing links that make many regular tilings or region shapes infeasible. As a result, multiprogramming and partitioning techniques that assume regular degree-4 grids or simple rectilinear regions cannot be directly applied on heavy-hex hardware, because such patterns either do not map cleanly to the available edges or leave qubits functionally isolated at region boundaries.

**Rigetti Square-Lattice Topology.** Rigetti’s Ankaa-3 processor (84 qubits) adopts a square-lattice topology [32] in which interior qubits exhibit four-fold connectivity. This regular structure closely resembles an ideal two-dimensional grid, enabling straightforward rectangular tiling and simplifying circuit routing compared to more irregular coupling maps. In addition, Rigetti’s architecture incorporates tunable couplers, which allow the effective inter-qubit coupling strength to be dynamically adjusted and can be leveraged to mitigate crosstalk in ways not possible with fixed-coupling designs.

The regularity of the square lattice makes it a natural testbed for early multiprogramming and partitioning approaches, many of which implicitly assume grid-like connectivity when defining region shapes. However, geometric regularity alone does not imply uniform execution quality. Similar to IBM devices, Rigetti processors exhibit substantial spatial variation in two-qubit gate fidelity and crosstalk across the chip. As a result, even on square-lattice hardware, static geometric partitioning fails to capture quality heterogeneity, motivating quality-aware region formation irrespective of topology regularity.

**IQM Star-Connected Topology.** IQM’s processors, including the 20-qubit Garnet and 54-qubit Emerald [14], use a star-connected topology where central “hub” qubits connect to multiple peripheral qubits. This architecture optimises for all-to-all connectivity within small clusters while maintaining sparse inter-cluster connections. The native gate set includes the CZ gate with typical fidelities above 99%.

IQM’s topology is particularly interesting for QVM design: natural cluster boundaries already exist at hub-peripheral interfaces. However, fixed geometric partitioning would create uniform-sized regions regardless of quality variation within clusters.

**Implications for QVM Design.** These topologies illustrate that QVM region definitions cannot be fixed templates. Even in a similar generation like IBM Heron r1 and Heron r2 would have significant QVM division and region. A practical QVM layer must infer regions directly from the device graph so that it transfers across coupling structures without manual redesign. Moreover, connectivity alone is an insufficient objective: because calibrated two-qubit fidelity and crosstalk vary spatially, regions should be formed that are internally high-quality, while placing boundaries on low-quality or high-interference links to enable QoS differentiation and robust isolation. Finally, the partition must be dynamic, since calibration updates and transient defects continuously reshape both the effective connectivity and the quality landscape.

DYNQ satisfies these requirements with a single graph-based formulation. It constructs a quality-weighted coupling graph from calibration data and applies community detection to derive regions that adapt to topology, stratify by quality, and can be rediscovered as the device snapshot evolves.

## 2.4 Error Propagation and Crosstalk in Multi-Tenant Execution

Understanding error behaviour is essential for effective QVM partitioning, particularly in multi-tenant settings where multiple quantum programs execute concurrently on physically proximate hardware regions. Unlike classical computation, errors in quantum circuits do not remain locally confined. Imperfect operations introduce coherent and stochastic errors that propagate through entangling gates, accumulate with circuit depth, and, in shared hardware environments, can couple across nominal program boundaries. As a result, both intra-program error amplification and inter-program interference must be considered when designing isolation mechanisms for quantum virtual machines.

**Intra-program error propagation.** Within a single program, gate errors accumulate multiplicatively. For a circuit with  $d$  two-qubit gates each having error rate  $\epsilon$ , the overall success probability is approximately  $(1-\epsilon)^d \approx e^{-d\epsilon}$  for small  $\epsilon$ . This exponential decay explains why high-quality regions are critical: a region with half the error rate can support circuits twice as deep before reaching the same total error.

**Inter-program crosstalk.** More insidious for multi-tenant execution is crosstalk, namely interference between programs executing on nominally disjoint qubit regions. Even without shared qubits, adjacent regions influence each other through several mechanisms:

*ZZ coupling* represents residual always-on interaction between neighbouring transmon qubits, arising from their physical capacitive coupling [9]. When two qubits are in states  $|11\rangle$ , they accumulate a relative phase  $\phi_{ZZ} = 2\pi\xi_{ZZ}t$  where  $\xi_{ZZ}$  is the *ZZ* coupling strength (typically 10–100 kHz) and  $t$  is the idle time [9]. This phase accumulation occurs even when no gates are applied, causing errors in both programs simultaneously. *ZZ* coupling is strongest between directly-coupled qubits but extends to second neighbours through virtual photon exchange.

*Measurement crosstalk* occurs when reading out one qubit disturbs the state of neighbours [34]. The readout pulse drives a resonator coupled to the target qubit; it can leak into adjacent resonators, leading to partial measurement of neighbouring qubits. On some devices, measuring qubit  $i$  can flip the state of the neighbouring qubit  $j$  with probability 0.1–1%, corrupting the unmeasured qubit’s quantum information.

*Control line crosstalk* happens when microwave pulses intended for one qubit partially affect others sharing the same control electronics or physically proximate control lines [29]. A strong drive pulse on qubit  $i$  may induce a weak (1–5%) spurious rotation on qubit  $j$  [41]. This is particularly problematic when different tenants’ programs apply gates simultaneously.

**Crosstalk and QVM boundary placement.** Effective QVM isolation requires boundaries that interrupt dominant error propagation paths rather than arbitrary geometric separations. In superconducting devices, the physical mechanisms responsible for inter-program crosstalk also degrade two-qubit gate fidelity, since both arise from strong residual coupling, frequency proximity, and shared control infrastructure. As a result, low-fidelity couplers identify links that are simultaneously computationally inefficient and prone to cross-region interference.

DYNQ encodes this principle directly in its graph model. By weighting couplers according to calibrated two-qubit fidelity, community detection preferentially cuts along the weakest and noisiest links, yielding regions that are internally cohesive for high-quality execution while naturally attenuating inter-tenant interference at their boundaries.

## 2.5 Transient Hardware Defects

A critical but often underappreciated challenge for QVM systems is the prevalence of transient hardware defects. Unlike permanent fabrication defects, which can be identified and avoided offline, transient defects arise dynamically during device operation and can temporarily render otherwise functional qubits or couplers unreliable. These effects fundamentally undermine static assumptions about hardware availability and gate quality.

One major source of transient defects is calibration drift. Qubit frequencies and gate parameters evolve between calibration cycles due to slow environmental changes, charging effects, and material relaxation. As a result, two-qubit gates that are initially calibrated to high fidelity can degrade significantly within a single calibration window, or fail entirely if frequency drift moves the interaction off resonance. Although periodic calibration resets these parameters, defects may emerge unpredictably mid-cycle, leaving the effective device graph inconsistent with its nominal specification. Additional transient behaviour arises from microscopic two-level system (TLS) fluctuators present in substrates and Josephson junction barriers. These parasitic quantum systems can intermittently couple to nearby qubits when their frequencies drift into resonance, causing abrupt reductions in coherence times. Such events are stochastic in nature, can persist from minutes to days, and may reduce qubit lifetimes by an order of magnitude without warning. Environmental perturbations further exacerbate this variability, including correlated quasiparticle bursts induced by cosmic rays or natural radioactivity, as well as spatially non-uniform thermal fluctuations, which can transiently degrade coherence and gate performance across large regions of the chip. [17, 22].

For QVM systems, the implications of these transient defects are severe. Static partitioning approaches, such as template-based region definitions, assume stable connectivity and uniform availability within each region. In practice, a single degraded coupler or qubit can render an entire predefined region invalid, leaving the compiler unable to route around the defect. In our experiments, such events result in complete execution failures and zero observed fidelity when circuits traverse affected regions. Across real devices, we observe failure rates consistent with transiently impaired regions affecting approximately 5–10% of static allocations at any given time.

DYNQ addresses this challenge by treating hardware state as dynamic rather than static. Regions are derived from the current calibration snapshot, with disabled qubits removed from the graph and degraded couplers assigned low or zero weight. Community detection then naturally routes regions around transient defects instead of through them. When calibration data updates, re-running region discovery requires only 0.81 seconds, producing an updated set of QVM regions that reflect the current hardware conditions and restore availability without manual intervention.

## 2.6 Quantum Cloud Cost Models and Multiprogramming

Quantum cloud pricing models play a central role in shaping the economic incentives for multiprogramming. On current platforms such as IBM Quantum, users are charged per *job time-consuming*, where each job executes a circuit or batch of circuits for a fixed number of shots, typically in the range of 1024–4096. Importantly, the cost of a job is largely independent of the number of qubits used by the circuit. As a result, a small circuit occupying a few qubits incurs the same cost as a much larger circuit scheduled on the same backend.

This pricing structure creates a strong incentive for multi-tenant execution at the cloud level. By serving multiple independent user workloads within a single job submission, the provider can amortise the cost of quantum hardware across tenants, improving utilisation, increasing throughput, and reducing queueing delays. From the provider’s perspective, multiprogramming transforms quantum processors from single-tenant, batch-oriented resources into shared infrastructure more closely resembling classical cloud systems.

From the user’s perspective, however, these benefits should be exposed through an abstraction rather than manual batching. Users typically submit individual circuits or workflows and expect the system to schedule them efficiently without requiring explicit coordination with other tenants. Quantum multiprogramming, implemented through a QVM layer, provides this abstraction by automatically combining independent circuits into a shared execution while preserving isolation and execution fidelity.

Concretely, consider a workload consisting of  $N$  independent circuits. The execution cost differs fundamentally under the two execution regimes:

- **Sequential execution:** each circuit is submitted as an individual job, resulting in  $N$  job submissions and a total cost proportional to  $N$ .
- **Batched execution via QVM multiprogramming:** up to  $k$  circuits are combined into a single job, yielding approximately  $\lceil N/k \rceil$  job submissions and a total cost proportional to  $N/k$ .

This corresponds to a cost reduction factor of  $k$ . For example, batching ten circuits per job reduces submission cost by approximately 90%. These economic gains are meaningful only if multiprogramming preserves execution quality, a property we evaluate empirically in Section 4.5.

At the system level, quantum multiprogramming using QVM assigns each circuit to a disjoint physical region of the processor. For circuits  $C_1, \dots, C_k$  requiring  $n_1, \dots, n_k$  logical qubits, a valid assignment maps each  $C_i$  to a region  $R_i$  such that  $|R_i| \geq n_i$ , the subgraph induced by  $R_i$  is connected, and regions are pairwise disjoint to ensure isolation. Connectivity is essential because physical paths within each region must support logical two-qubit interactions. Sparse or poorly connected regions incur additional routing overhead through SWAP operations, increasing circuit depth and error accumulation. Consequently, effective multiprogramming using QVM requires not only sufficient qubit count but also high-quality internal connectivity within each assigned region.

## 2.7 Limitations of Existing QVM Approaches

Prior work uses the term *quantum virtual machine* to describe several mechanisms that improve the efficiency of quantum clouds. One major direction is spatial multiplexing (quantum multi-programming), where multiple independent circuits are mapped to disjoint chip subsets and executed concurrently to increase utilisation and reduce queueing delay [8, 20, 21, 25]. A complementary direction introduces provider-side virtual regions as a runtime abstraction, allowing tenants to compile independently while the cloud assigns jobs to the predefined areas at execution time [38]. A third, largely orthogonal, body of work explores gate virtualisation and circuit fragmentation to scale a *single* computation beyond device size or connectivity limits [40]. Together, these lines demonstrate the promise of virtualisation, but they also expose structural gaps when viewed as a practical, multi-tenant cloud layer.

**Batch-coupled placement and compilation.** A recurring theme across multi-programming systems is tight coupling between batching, compilation, and placement. Many proposals implicitly assume that the set of co-running programs is known at mapping time, because partitioning and routing decisions are optimised for a specific batch composition [8, 20, 25]. While reasonable for offline evaluations, this assumption is restrictive in cloud settings where workloads arrive asynchronously and the scheduler must balance latency, throughput, and fairness. As a result, the abstraction remains batch-specific rather than a stable, reusable, and consistently managed virtual resource across workload instances.

**Topology-bound virtualisation and limited portability.** Several QVM designs achieve high performance by exploiting detailed knowledge of the coupling graph through hand-crafted region templates or topology-tailored heuristics [20, 38]. HyperQ, for example, formalises the virtual-region abstraction and demonstrates efficient tiling on a target topology [38]. However, such designs do not generalise seamlessly as processor architectures diversify: region definitions and placement heuristics must be redesigned or retuned for each new coupling structure, creating an increasing engineering burden and limiting portability across hardware generations [21].

**Brittleness under dynamic calibration and transient defects.** Cloud-ready virtualisation must remain robust as the effective device graph evolves across calibration cycles and within calibration windows. In practice, qubits or couplers can degrade or become unavailable due to drift and transient defects, reshaping feasible connectivity without warning. Static region definitions are brittle under these dynamics: a single degraded link can invalidate an entire region, leading to allocation failures or excessive rerouting [38]. Compiler-based multi-programming often incorporates calibration data into one-shot mappings, but typically treats re-partitioning as an offline or exceptional process rather than a routine runtime operation, leaving a gap between hardware reality and the assumptions embedded in current abstractions [20, 25].

**Quality-agnostic resource models and coarse isolation.** Many approaches ensure feasibility by enforcing connectivity and disjointness, and some incorporate crosstalk-aware heuristics, yet they largely treat feasible regions as interchangeable [21, 25]. On real devices, two-qubit gate fidelities and interference profiles vary substantially across a single chip. Provider-side isolation mechanisms such as reserving fixed buffer qubits between regions [38] can suppress interference, but they are inherently static: they do not adapt to spatial quality variations or transient calibration changes, and they may waste high-fidelity qubits by dedicating them to separation rather than computation. The absence of an explicit, quality-stratified resource model limits the ability of existing QVMs to provide differentiated service levels and to suppress inter-tenant interference as concurrency increases systematically.

**Scale-up virtualisation is orthogonal to multi-tenancy.** Gate virtualisation techniques address the challenge of executing a single computation beyond hardware limits by transforming and distributing interactions [38]. While powerful, these methods target a different axis of scalability and do not directly address concurrent isolation, dynamic reconfiguration from calibration snapshots, or quality-aware placement within a shared device.

Taken together, existing QVM approaches illustrate the benefits of virtualisation but stop short of providing a unified cloud abstraction that is portable across topologies, resilient to calibration dynamics, and explicit about hardware quality. These gaps motivate a QVM design that treats the calibrated device graph as runtime state, derives virtual regions algorithmically rather than from fixed templates, and decouples tenant submission from placement decisions.

## 3 Design

DYNQ instantiates the QVM abstraction through a principled two-phase architecture: *offline discovery* transforms hardware calibration data into a pool of quality-stratified virtual machines, while *online allocation* maps tenant programs to available QVMs at runtime. This separation mirrors classical virtualisation: the hypervisor manages physical resources (offline) while presenting virtualised interfaces to guests (online).

The key design principle is **high cohesion, low coupling**, which is borrowed from software engineering and classical systems design. Within each QVM region, we maximise internal connectivity (cohesion) to enable efficient circuit compilation with minimal SWAP overhead. Between regions, we minimise connection strength (coupling) to suppress crosstalk interference between tenants. The Louvain community detection algorithm naturally optimises this objective by maximising modularity.

This section details the architecture, then each algorithmic component.

### 3.1 System Architecture Overview

Figure 2 presents the layered architecture of DYNQ, which is designed to separate topology- and quality-dependent analysis from latency-critical runtime decisions. This separation allows DYNQ to adapt to evolving hardware conditions while providing fast, predictable allocation for incoming workloads. At a high level, the system decomposes QVM functionality into four layers, each responsible for a distinct stage of abstraction and decision-making.

At the lowest level, the *hardware abstraction layer* constructs a uniform representation of the underlying quantum processor. The `HardwareGraph` module extracts calibrated qubit and coupler properties, such as coherence times, readout errors, and two-qubit gate fidelities, from the backend calibration interface. These properties are encoded as a weighted graph, with vertices representing qubits and edges representing native couplers. By abstracting hardware as a graph parameterised by calibrated quality metrics, DYNQ decouples all subsequent algorithms from backend-specific details and enables the same pipeline to operate across heterogeneous quantum processors.

Above this abstraction, DYNQ performs *offline region discovery*, an analysis stage amortised over each calibration cycle. At this stage, the system identifies candidate execution regions that are internally well-connected and externally weakly coupled, termed QVM atomic regions. The `CommunityDetector` applies modularity-based community detection to the weighted hardware graph, producing a set of densely connected subgraphs. These candidate regions are then evaluated by the `RegionScorer` using multiple quality indicators, including internal gate fidelity and boundary weakness. Finally, the `RegionSelector` resolves overlaps and selects a non-overlapping subset, yielding a pool of pre-validated QVM regions annotated with quality scores. Because this process is executed offline, DYNQ can employ computationally intensive analysis without affecting runtime latency.

The *online allocation layer* handles real-time scheduling decisions for incoming circuits. Given a circuit request, the `QVMAllocator` selects a suitable QVM from the precomputed pool using a fitness function that balances circuit requirements against region quality and availability. The `AllocationState` maintains the current occupancy of QVM atomic regions, ensuring isolation between concurrent tenants. `Multi-Region Composer` will try to composite a large QVM using small QVM atomic regions. When no suitable region is immediately available, the `DeferredRetryScheduler` defers the circuit to a subsequent batch, enabling graceful handling of contention without blocking the system. This design ensures that runtime allocation remains lightweight while still exploiting the richer structure discovered offline.

Finally, the *execution layer* is responsible for assembling and running multi-tenant workloads. The `CircuitCompiler` forwards each circuit to a standard compilation backend, such as Qiskit’s default `qiskit.transpiler`, together with the topology and calibration metadata of the assigned QVM region. The compiler then performs region-restricted transpilation, and the resulting compiled circuit is collected and returned to the execution layer. The `CircuitCombiner` merges the circuits assigned to distinct QVM regions into a single composite circuit that preserves logical isolation. This composite circuit is remapped and submitted to the backend by the `QiskitBackendRunner`. After execution, the `ResultDemultiplexer` separates measurement outcomes and returns results to individual tenants transparently, i.e., via a reverse-remapping process, to obtain the results of each QVM. From the user’s perspective, each circuit executes independently, while the system internally realises the efficiency gains of concurrent

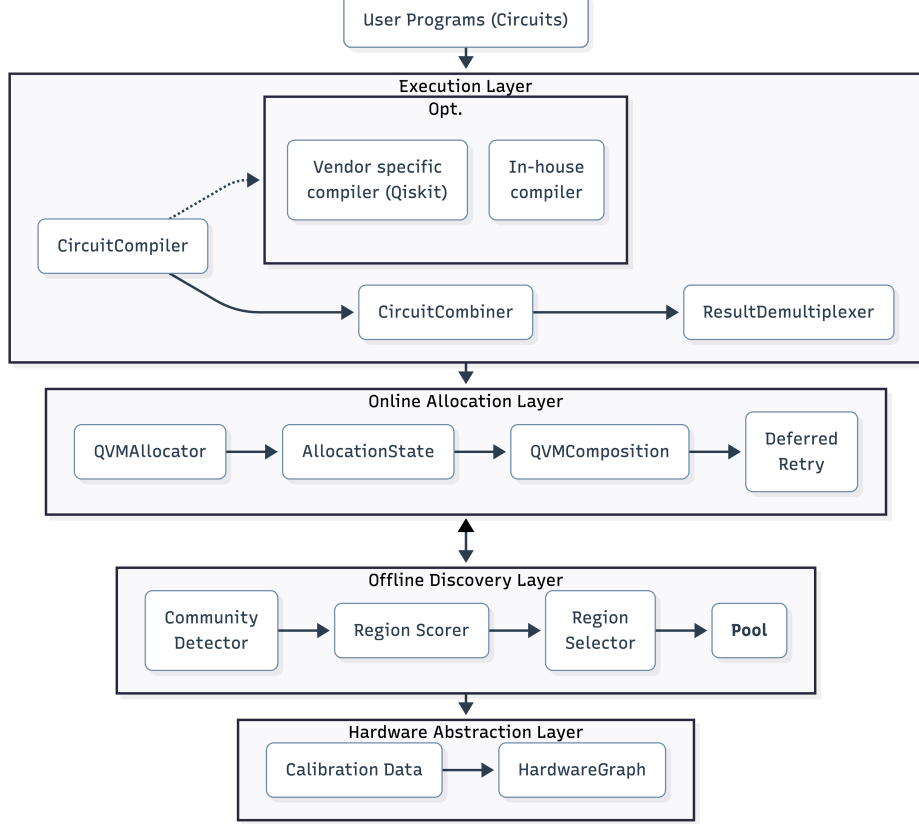


Figure 2: **The layered architecture of DynQ.** The design explicitly decouples computationally intensive topology analysis (*Offline Discovery Layer*) from latency-critical scheduling decisions (*Online Allocation Layer*). By abstracting physical device properties into a **HardwareGraph**, the system maintains a pool of pre-validated QVM atomic regions to efficiently service incoming user programs.

execution.

### 3.2 Hardware Graph Construction

We model the quantum processor as a weighted undirected graph  $G = (V, E, w)$ . Vertices  $V$  represent physical qubits, edges  $E$  represent couplers that enable two-qubit gates, and the weight function  $w : E \rightarrow \mathbb{R}^+$  encodes gate quality.

We define edge weights as the inverse of gate error rates:

$$w_{ij} = \frac{1}{\epsilon_{ij} + \epsilon_0} \quad (1)$$

where  $\epsilon_{ij}$  is the two-qubit gate error rate for the coupler between qubits  $i$  and  $j$ , and  $\epsilon_0 = 10^{-6}$  is a small regularisation constant to avoid numerical instability. Here,  $\epsilon_{ij}$  can be instantiated as the *RB-derived average two-qubit gate infidelity* reported by the backend calibration interface. We note that community detection depends only on relative edge weights; any monotonic transformation of gate error rates yields equivalent partitions. This inverse relationship ensures that high-fidelity gates receive high weights: a coupler with 0.5% error receives weight approximately 200, while one with 1% error receives weight approximately 100. The ratio of weights equals the inverse ratio of error rates, so a coupler twice as reliable has twice the weight.

This weighting scheme has a natural interpretation in terms of circuit fidelity. For a circuit using  $k$  two-qubit gates, the overall success probability is approximately  $\prod_{i=1}^k (1 - \epsilon_i) \approx e^{-\sum_i \epsilon_i}$  for small error rates, although two-qubit errors are not strictly independent Bernoulli events [33]. Total minimising mistake is equivalent to minimising  $\sum_i \epsilon_i$ , which our weighting encourages by favouring high-weight (low-error) edges.

The weighted graph naturally handles hardware defects without special-case logic. Disabled qubits are simply absent from the vertex set  $V$ ; broken couplers are absent from the edge set  $E$ . When community detection is applied

to this graph, it observes only functional hardware and partitions accordingly. Defects automatically become region boundaries because no edges cross them. This property is crucial for handling transient defects: by rebuilding the graph from current calibration data, DYNQ automatically routes around problematic regions. This design eliminates the need for explicit fault-handling heuristics at higher layers, allowing defect tolerance to emerge directly from the graph abstraction.

Graph construction requires a single pass over calibration data and runs in  $O(|V| + |E|)$  time. On a 156-qubit heavy-hex processor [13], this overhead is negligible compared to the calibration interval.

### 3.3 Community Detection: Formalising High Cohesion, Low Coupling

Effective QVM partitioning can be cast as a graph-structural objective. Within each QVM atomic region, qubits should be connected by high-quality couplers to support efficient compilation and limit SWAP overhead, while connections across regions should be weak so as to attenuate crosstalk and residual interactions between concurrent programs. In graph-theoretic terms, this corresponds to partitions with strong intra-regional connectivity and weak inter-regional connectivity.

Community detection provides a natural and principled mechanism for constructing such partitions. By optimising for densely connected subgraphs that are sparsely linked to one another, community detection directly captures the isolation and locality requirements of multi-tenant quantum execution. This formulation aligns with a long-standing principle in classical systems design, where modular structures are preferred for their strong internal coherence and limited external interaction. In DYNQ, modularity-maximising community detection operationalises this principle as an explicit optimisation objective over the physical coupling graph.

We use the Louvain algorithm [5], a measure of how well a partition captures community structure, to optimise modularity. For a partition of graph  $G$  into communities, modularity is defined as:

$$Q = \frac{1}{2W} \sum_{i,j} \left[ w_{ij} - \frac{s_i s_j}{2W} \right] \delta(c_i, c_j) \quad (2)$$

where  $w_{ij}$  is the edge weight between vertices  $i$  and  $j$  (zero if no edge exists),  $s_i = \sum_j w_{ij}$  is the weighted degree of vertex  $i$ ,  $W = \frac{1}{2} \sum_{i,j} w_{ij}$  is the total edge weight in the graph, and  $\delta(c_i, c_j)$  equals 1 if vertices  $i$  and  $j$  belong to the same community and 0 otherwise. Here,  $Q$  is a scalar objective that measures the quality of the partition, with larger values indicating stronger community structure. The modularity objective admits a straightforward interpretation. The term  $w_{ij}$  accounts for the actual edge weight placed within communities, while  $\frac{s_i s_j}{2W}$  represents the expected weight under a null model that preserves the weighted degree sequence. Modularity, therefore, measures the excess internal connectivity of a partition relative to random chance.

When applied to a quality-weighted hardware graph, this objective directly benefits QVM partitioning. Maximising modularity preferentially groups qubits connected by high-weight edges, corresponding to low-error couplers, into the same community, while edges with low weight contribute little to the objective and are more likely to lie across community boundaries. In effect, the optimisation encourages regions whose internal connectivity is supported by high-fidelity gates, while naturally placing partition boundaries along noisy or unreliable couplers. This behaviour is not imposed heuristically but emerges directly from the modularity function's structure.

The Louvain algorithm optimises modularity through a greedy agglomerative process with two alternating phases.

**Local optimisation.** The algorithm iteratively refines an initial partition by relocating individual vertices to neighbouring communities whenever doing so yields a positive modularity gain. This phase rapidly increases modularity by exploiting local structure in the graph and converges when no further-improving moves remain. In the context of DYNQ's quality-weighted hardware graph, this process preferentially groups qubits connected by high-fidelity couplers, since such moves yield the largest immediate modularity gains.

**Aggregation.** Once local optimisation stabilises, communities are contracted into super-vertices to form a coarsened graph, with edge weights aggregated accordingly. Modularity optimisation is then repeated on this reduced graph, enabling the algorithm to capture higher-level community structure beyond local optima. For DYNQ, this hierarchical aggregation produces execution regions that remain cohesive across scales, allowing region boundaries to stabilise around consistently weak or noisy couplers rather than transient local fluctuations. These two phases alternate until modularity no longer improves.

This hierarchical optimisation strategy balances solution quality with computational efficiency. Local moves exploit fine-grained structure, while aggregation enables global reorganisation at progressively coarser scales. In practice, the algorithm converges quickly on sparse graphs with community structure. On a 156-qubit heavy-hex

hardware graph, region discovery completes in under 100 ms, making it suitable for execution once per calibration cycle.

### 3.4 Region Scoring

Not all discovered communities are equally suitable as QVM atomic regions. Community size directly affects both practical usability and scheduling flexibility in a multi-tenant setting. Very small communities, while potentially useful for trivial circuits or diagnostics, offer limited capacity and tend to increase fragmentation in the region pool. Conversely, very large communities may span heterogeneous quality zones, mixing high- and low-fidelity couplers in a way that undermines quality-aware placement. To balance flexibility, usability, and robustness, we retain communities with at least three qubits and evaluate the remainder using multiple complementary quality metrics that capture distinct aspects of region suitability.

For a candidate region  $R$  (a connected subgraph with vertex set  $V_R$  and edge set  $E_R$ ), we compute four scores:

**Connectivity score.** Measures how densely connected the region is internally:

$$S_{\text{conn}}(R) = \frac{2|E_R|}{|V_R|(|V_R| - 1)} \quad (3)$$

This is the ratio of actual edges to the maximum possible edges in a complete graph. For a fully-connected region,  $S_{\text{conn}} = 1$ ; for a linear chain of  $n$  qubits,  $S_{\text{conn}} = 2/(n - 1)$ . Higher connectivity means more routing options during circuit compilation, reducing SWAP overhead. On heavy-hex topology, typical regions achieve  $S_{\text{conn}}$  between 0.2 and 0.5.

**Gate quality score.** Captures the average two-qubit gate fidelity:

$$S_{\text{gate}}(R) = \max(0, 1 - 100 \cdot \bar{\epsilon}_{\text{gate}}) \quad (4)$$

where  $\bar{\epsilon}_{\text{gate}} = \frac{1}{|E_R|} \sum_{(i,j) \in E_R} \epsilon_{ij}$  is the mean gate error rate across all couplers in  $R$ . The scaling factor 100 maps typical error rates to a 0–1 score: 0.5% error yields  $S_{\text{gate}} = 0.5$ , while 1.5% error yields near zero. This score directly reflects the dominant error source in NISQ circuits.

**Readout quality score.** Captures measurement fidelity:

$$S_{\text{ro}}(R) = \max(0, 1 - 10 \cdot \bar{\epsilon}_{\text{ro}}) \quad (5)$$

where  $\bar{\epsilon}_{\text{ro}} = \frac{1}{|V_R|} \sum_{i \in V_R} \epsilon_{\text{ro},i}$  is the mean readout error across qubits in  $R$ . The scaling factor differs from gate quality because readout errors are typically larger (1–5% versus 0.3–3% for gates). Readout fidelity affects the final measurement step of every circuit and cannot be mitigated through circuit optimisation.

**Uniformity score.** Penalises internal variation in two-qubit gate quality:

$$S_{\text{unif}}(R) = \max(0, 1 - \text{CV}_{\text{gate}}(R)), \quad (6)$$

where

$$\text{CV}_{\text{gate}}(R) = \frac{\sigma_{\epsilon}}{\mu_{\epsilon}} \quad (7)$$

is the coefficient of variation of two-qubit gate error rates within region  $R$ . Here,  $\mu_{\epsilon} = \frac{1}{|E_R|} \sum_{(i,j) \in E_R} \epsilon_{ij}$  and  $\sigma_{\epsilon} = \sqrt{\frac{1}{|E_R|} \sum_{(i,j) \in E_R} (\epsilon_{ij} - \mu_{\epsilon})^2}$  denote the mean and standard deviation of two-qubit gate error rates within region  $R$ , respectively. High uniformity, corresponding to low variation, indicates that all couplers in the region exhibit similar error rates, allowing the compiler to apply consistent optimisation strategies. By contrast, a region containing both very low-error and very high-error couplers may exhibit acceptable average quality but poor uniformity, limiting the compiler’s ability to exploit high-quality interactions without incurring errors from weaker ones.

The composite quality score combines these metrics as a weighted sum:

$$Q(R) = 0.25 \cdot S_{\text{conn}} + 0.35 \cdot S_{\text{gate}} + 0.20 \cdot S_{\text{ro}} + 0.20 \cdot S_{\text{unif}}. \quad (8)$$

Gate quality is assigned the highest weight, reflecting the fact that two-qubit gate errors typically dominate overall circuit fidelity on current NISQ hardware. Connectivity is given the second-highest weight, as limited connectivity directly increases SWAP overhead and circuit depth. Readout fidelity and uniformity are treated as secondary factors and share the remaining weight. We note that these weights are chosen heuristically to reflect prevailing hardware characteristics, and alternative weightings or task-specific reparameterisations could be explored in future work.

---

**Algorithm 1** Greedy Region Selection

---

**Require:** Candidate regions  $\{R_1, \dots, R_m\}$  with scores  $Q(R_i)$

**Ensure:** Selected regions  $\mathcal{S}$

```

1: Sort candidates by  $Q(R_i)/|R_i|$  in descending order
2:  $\mathcal{S} \leftarrow \emptyset$ ; used  $\leftarrow \emptyset$ 
3: for each  $R$  in sorted order do
4:   if  $R \cap \text{used} = \emptyset$  then
5:      $\mathcal{S} \leftarrow \mathcal{S} \cup \{R\}$ 
6:     used  $\leftarrow \text{used} \cup R$ 
7:   end if
8: end for
9: return  $\mathcal{S}$ 

```

---

### 3.5 QVM Atomic Region Selection

Community detection typically yields a QVM atomic region *pool* that contains (i) overlapping candidates arising from the hierarchical refinement of partitions and (ii) more candidates than can be instantiated simultaneously on the same processor. The scheduling layer therefore requires a *non-overlapping* subset of QVM atomic regions that achieves high aggregate quality while preserving sufficient flexibility for subsequent allocation.

Formally, let  $\{R_i\}_{i=1}^m$  denote the set of candidate QVM atomic regions, where each region  $R_i$  is associated with a quality score  $Q(R_i)$  and occupies a set of physical qubits  $V(R_i) \subseteq V$ . The region selection problem is defined as:

$$\begin{aligned} \max_{\mathcal{S} \subseteq \{R_1, \dots, R_m\}} \quad & \sum_{R \in \mathcal{S}} Q(R) \\ \text{s.t.} \quad & V(R_i) \cap V(R_j) = \emptyset, \quad \forall R_i \neq R_j \in \mathcal{S}. \end{aligned} \quad (9)$$

This formulation corresponds to the weighted set packing problem and is NP-hard. Algorithm 1 shows the approach: we sort candidates by quality density (score per qubit), then greedily select non-conflicting regions.

Ranking by density biases selection toward compact high-quality regions and avoids a common failure mode in which a large but mediocre region blocks multiple smaller, higher-quality alternatives. To illustrate this, consider two competing selections that overlap in physical qubits. The first consists of a single region  $R_A$  with  $|V(R_A)| = 20$  and quality score  $Q(R_A) = 0.6$ , yielding a density of 0.03. The second consists of two disjoint regions  $R_B$  and  $R_C$ , each with  $|V| = 10$  and  $Q = 0.5$ , yielding densities of 0.05. Although  $R_A$  has higher absolute quality than either  $R_B$  or  $R_C$  individually, selecting  $R_A$  excludes both smaller regions. In contrast, selecting  $R_B$  and  $R_C$  achieves a higher total utility (1.0 versus 0.6) while preserving greater flexibility for subsequent allocation. Density-based ordering correctly prefers the latter outcome.

### 3.6 Online Allocation

At runtime, DYNQ maintains a pool of available QVM atomic regions (those not currently hosting executing programs) and services incoming allocation requests. The allocation policy must balance multiple objectives: matching program size to region size (avoiding waste), preferring high-quality regions for better fidelity, and ensuring fair access to the region pool.

For a request requiring  $n$  qubits, DYNQ evaluates each available region  $R$  using a fitness function:

$$F(R, n) = 0.2 \cdot S_{\text{size}}(R, n) + 0.4 \cdot S_{\text{conn}}(R) + 0.4 \cdot Q(R) \quad (10)$$

We explicitly retain  $S_{\text{conn}}$  as a separate term to bias runtime allocation toward regions that minimises routing overhead for the specific circuit, complementing the offline quality score  $Q(R)$ , which aggregates multiple static calibration metrics.

The size score implements a best-fit policy that penalises waste:

$$S_{\text{size}}(R, n) = \begin{cases} 0 & \text{if } |R| < n \\ 1 & \text{if } |R| = n \\ e^{-0.5(|R|-n)/n} & \text{if } |R| > n \end{cases} \quad (11)$$

Undersized QVM atomic regions receive a score of 0 (a hard constraint, meaning they cannot host the circuit). Exact-fit regions receive the maximum score. Oversized regions are penalised exponentially: a region 50% larger

than needed scores  $e^{-0.25} \approx 0.78$ ; one twice the needed size scores  $e^{-0.5} \approx 0.61$ . This encourages the use of appropriately sized regions while allowing oversized allocations when necessary.

Allocation proceeds atomically as follows: (1) scan available QVM atomic regions, computing fitness for each; (2) select the region with the highest fitness; (3) mark the selected region as busy; (4) return a mapping working inside the QVM from logical qubits (0 to  $n - 1$ ) to physical qubits within the region. Upon program completion, the QVM atomic region returns to the available pool.

### 3.7 Multi-Region Composition for Large Circuits

**Motivation.** Online allocation in Section 3.6 selects a *single* available QVM atomic region. This fails when the offline pool intentionally favours compact, high-cohesion QVM atomic regions: the chip may have enough free qubits in aggregate, yet no single free QVM atomic region can satisfy  $|R| \geq n$ . A QVM that is composed by multi-region composition is an online fallback that merges multiple *available* QVM atomic regions into one *connected* footprint, preserving the same isolation guarantee as subgraph-restricted compilation (Section 3.9). The multi-region composition step is to close the fragmentation gap.

**Formulation.** Let  $\mathcal{R}_{\text{free}}$  be the set of currently-available atomic regions and let the request require  $n$  qubits. We seek  $\mathcal{C} \subseteq \mathcal{R}_{\text{free}}$  such that  $V(\mathcal{C}) = \bigcup_{R \in \mathcal{C}} V(R)$  satisfies: (i)  $|V(\mathcal{C})| \geq n$  (capacity), (ii) regions are disjoint (inherited from the pool and availability), (iii) the induced subgraph  $G[V(\mathcal{C})]$  is connected (hard constraint), and (iv) bridge-induced quality loss is explicitly penalised.

**Bridge-aware greedy composition.** To fulfil resource requests that exceed the capacity of a single atomic region, DYNQ employs a multi-region composition strategy. We lift the hardware graph into a region-adjacency view, where two regions  $R_i$  and  $R_j$  are adjacent if there exists at least one coupler crossing their boundary. We define the *bridge edge set* between them as:

$$E_B(R_i, R_j) = \{(q_a, q_b) \in E : q_a \in V(R_i), q_b \in V(R_j)\}. \quad (12)$$

Since community detection algorithms often use weaker couplers as natural boundaries for partitioning, these inter-region bridges represent a critical bottleneck to fidelity and must be explicitly scored.

Finding the exact optimal connected subgraph is NP-hard. Consequently, we adopt a heuristic approach detailed in Algorithm 2. The process starts with a high-quality “seed” region and iteratively expands the footprint by attaching the optimal adjacent region.

The marginal score  $s$  (Line 9) balances three factors: the intrinsic quality  $Q(R)$ , the structural integrity of the *combined* footprint  $S_{\text{conn}}$ , and the interface quality  $S_{\text{bridge}}$ . The weights (0.4, 0.4, 0.2) mirror the allocation policy in Section 3.6, where the *bridge* score replaces the *size* score as the scenario-specific constraint. We define  $S_{\text{bridge}}(E_B)$  by applying the gate quality score metric (Eq. 4) to the bridge set  $E_B$ :

$$S_{\text{bridge}}(E_B) = \max \left( 0, 1 - 100 \cdot \frac{1}{|E_B|} \sum_{(i,j) \in E_B} \epsilon_{ij} \right). \quad (13)$$

This formulation ensures that the expansion prioritises regions connected by high-fidelity couplers, preventing the formation of weak links in the composed QVM.

This keeps composition decisions aligned with the paper’s global quality semantics: prefer high QVM atomic regions, but reject merges that rely on weak boundary couplers, and avoid shapes with poor routing flexibility (low induced  $S_{\text{conn}}$ ).

**Integration, compilation, and trade-offs.** If the greedy construction returns a connected footprint  $V$ , DYNQ materialises a temporary composed region  $\widehat{R}$  with  $V(\widehat{R}) = V$  and coupling map given by the induced subgraph  $G[V]$ . The allocator treats  $\widehat{R}$  as a candidate region using the same size-matching and fitness logic as Section 3.6; on acceptance, all constituent atomic regions are marked busy and released together. Compilation remains strictly subgraph-restricted to  $G[V]$  (Section 3.9). To mitigate boundary bottlenecks, DYNQ additionally exposes bridge metadata (bridge edges/qubits and component boundaries) to guide initial layout and routing heuristics.

*Example.* For a 12-qubit request where the largest free QVM atomic region has 8 qubits, composition seeds with  $R_A$  ( $|R_A| = 8$ ,  $Q(R_A) = 0.75$ ). Two adjacent candidates are  $R_B$  ( $|R_B| = 5$ ,  $Q = 0.70$ , stronger bridges) and  $R_C$  ( $|R_C| = 4$ ,  $Q = 0.80$ , weaker bridges). Despite higher  $Q$  for  $R_C$ , the marginal score selects  $R_B$  due to better bridge

---

**Algorithm 2** Greedy QVM Multi-Region Composition

---

**Require:** Available regions  $\mathcal{R}_{\text{free}}$ , target size  $n$ , hardware graph  $G$   
**Ensure:** Composed footprint  $V$  (as a union of regions) or  $\perp$

```

1: Choose seed  $R_{\text{seed}} \in \mathcal{R}_{\text{free}}$  (largest-first);  $\mathcal{C} \leftarrow \{R_{\text{seed}}\}$ ;  $V \leftarrow V(R_{\text{seed}})$ 
2: while  $|V| < n$  do
3:    $R^* \leftarrow \perp$ ;  $s^* \leftarrow -\infty$ 
4:   for  $R \in \mathcal{R}_{\text{free}} \setminus \mathcal{C}$  do
5:     if  $V(R) \cap V \neq \emptyset$  then
6:       continue
7:     end if
8:      $E_B \leftarrow \{(u, v) \in E : u \in V, v \in V(R)\}$                                  $\triangleright$  Bridges to current footprint
9:     if  $E_B = \emptyset$  then
10:      continue
11:    end if
12:     $s \leftarrow 0.4 Q(R) + 0.4 S_{\text{conn}}(G[V \cup V(R)]) + 0.2 S_{\text{bridge}}(E_B)$ 
13:    if  $s > s^*$  then
14:       $R^* \leftarrow R$ ;  $s^* \leftarrow s$ 
15:    end if
16:   end for
17:   if  $R^* = \perp$  then
18:     return  $\perp$ 
19:   end if
20:    $\mathcal{C} \leftarrow \mathcal{C} \cup \{R^*\}$ ;  $V \leftarrow V \cup V(R^*)$ 
21: end while
22: if  $G[V]$  is disconnected then
23:   return  $\perp$ 
24: end if
25: return  $V$ 

```

---

quality and resulting connectivity, yielding  $|V| = 13$  and admitting the circuit. The quality tradeoff is explicit: the composed footprint is feasible, but bridge penalties quantify why it is typically weaker than the best single region.

Composition is a fallback: it can reduce quality (bridges are usually weaker), increase routing overhead (boundary chokepoints), and span a larger physical area (potentially more correlated noise exposure). In exchange, it converts fragmentation-induced allocation failures into feasible placements while preserving the same isolation and compilation model.

**Overhead.** With  $k$  free regions and average region size  $\bar{n}$ , each greedy step scans  $O(k)$  candidates and evaluates bridge/connectivity statistics in  $O(\bar{n})$ , for  $O(k^2\bar{n})$  worst-case time plus a linear-time connectivity check on  $G[V]$ . In practice (tens of regions), this adds millisecond-level overhead to the allocation path.

### 3.8 Deferred Retry Scheduling

In a multi-tenant setting, not all circuits can be allocated to every execution batch when the QVM is composed of multiple regions. Temporary resource contention may leave no suitable region available even when a circuit is compatible with the hardware. Rejecting such requests immediately would unnecessarily reduce system utilisation and penalise bursty workloads. To address this, DYNQ introduces a *two-level deferred retry mechanism* that explicitly separates transient contention from fundamental infeasibility.

**Problem setting.** The allocation problem addressed by DYNQ is inherently dynamic. Circuit requests arrive over time with heterogeneous qubit requirements for the QVM region, while any regions are released only at batch boundaries after previously admitted circuits complete. As a result, allocation decisions must be made without knowledge of future arrivals and without global rescheduling across batches.

In the common case, as illustrated by the Algorithm 3, circuits are admitted in the order of their arrival whenever sufficient resources (QVM region or QVM atomic region) are available. When a circuit cannot be placed immediately due to temporary contention, it is preferable to defer the request rather than reject it outright, since feasibility may change once the current regions are freed. At the same time, the system must eventually distinguish between requests that are temporarily blocked and those that are fundamentally infeasible given the hardware limits.

---

**Algorithm 3** Deferred Retry Batch Scheduling

---

**Require:** Circuits  $\{C_1, \dots, C_N\}$ , max batch size  $B$   
**Ensure:** Executed circuits with allocation results

```

1: retry\_queue  $\leftarrow \emptyset$ 
2:  $i \leftarrow 0$ 
3: while  $i < N$  or  $\text{retry\_queue} \neq \emptyset$  do
4:   batch  $\leftarrow$  pop up to  $B$  circuits from  $\text{retry\_queue}$ 
5:   batch  $\leftarrow$  batch  $\cup$  next  $(B - |\text{batch}|)$  circuits from  $i$ 
6:   allocations  $\leftarrow$  Allocate(batch)
7:   for  $c \in \text{batch}$  not in allocations do
8:      $\text{retry\_queue.append}(c)$  ▷ Defer to next batch
9:   end for
10:  Execute(batch, allocations)
11:  Deallocate(allocations) ▷ Release regions
12:   $i \leftarrow i + |\text{new circuits in batch}|$ 
13: end while ▷ Final sweep for remaining retries
14:
15: for  $c \in \text{retry\_queue}$  do
16:   Try allocate and execute  $c$  individually
17: end for

```

---

The scheduler must therefore balance prompt admission, controlled deferral, and decisive resolution of infeasible requests, while avoiding speculative backtracking or repeated global repartitioning that would increase latency and complexity.

At the first level, *batch-level deferral* handles transient contention. Circuits that fail allocation in batch  $k$  are placed into a retry queue rather than being rejected. In the subsequent batch  $k + 1$ , deferred circuits are considered *before* newly arrived requests, granting them priority access to regions released at the end of batch  $k$ . This priority rule ensures that circuits delayed only by temporary occupancy are admitted promptly once resources become available, preventing starvation under bursty load.

At the second level, *global retry validation* distinguishes transient failure from hard infeasibility. After all regular batches have been processed, DYNQ performs a final retry sweep in which the entire region pool is available and no competing allocations exist. Circuits that still cannot be placed at this stage are guaranteed to exceed the capacity of every available QVM region and are therefore declared infeasible due to fundamental hardware limits rather than scheduling artefacts.

**Convergence properties.** Let  $C_{\text{fail}}^{(k)}$  denote the set of circuits that fail allocation in batch  $k$  under the batch-level retry policy. The two-level deferred retry mechanism exhibits the following convergence properties.

1. **Bounded retry queue evolution.** The size of the retry queue evolves according to

$$|C_{\text{fail}}^{(k+1)}| \leq |C_{\text{fail}}^{(k)}| + n_{\text{new}}, \quad (14)$$

where  $n_{\text{new}}$  denotes the number of newly arrived circuits in batch  $k + 1$ . In practice, the queue typically contracts rather than grows: deferred circuits are prioritised in the next batch, and all regions occupied in batch  $k$  are deterministically released before batch  $k + 1$  begins. This prevents unbounded accumulation caused solely by transient contention.

2. **Implicit size-based filtering.** Circuits in the retry queue are naturally filtered by size. Small and medium-sized circuits are highly likely to succeed upon retry because the offline selection process favours many compact, high-quality regions over a few large ones. In contrast, large circuits that exceed the capacity of most regions will continue to fail at the batch level and are deferred to the second retry stage. This behaviour emerges without explicit size thresholds or classification.

3. **Termination via global retry validation.** In the final retry sweep, the entire QVM atomic region pool is available and no competing allocations exist. Any circuit that fails at this stage must require more qubits than the largest available region, and is therefore infeasible due to fundamental hardware limits rather than scheduling effects, thereby guaranteeing termination of the retry process and preventing indefinite deferral.

Taken together, these properties ensure that the two-level retry mechanism converges efficiently for heterogeneous workloads. Circuits delayed by temporary resource contention are admitted promptly, often in the immediately subsequent batch, while genuinely infeasible requests are identified decisively in the global retry stage. As a result, deferred retry improves allocation success without introducing starvation or unbounded queue growth.

### 3.9 Hardware-Aware Compilation

After QVM region allocation, DYNQ performs hardware-aware compilation by transpiling each tenant circuit onto its assigned execution region. The core mechanism is *subgraph-restricted compilation*: for a selected region  $R$  with vertex set  $V_R$  and induced coupler set  $E_R$ , DYNQ constructs the induced coupling graph  $G_R = (V_R, E_R)$  of QVM region and invokes the Qiskit transpiler with (i) a restricted coupling map corresponding to  $G_R$  and (ii) an initial layout that maps logical qubits exclusively onto  $V_R$ . As a result, all routing, SWAP insertion, and scheduling decisions are confined to the allocated region by construction, providing strict spatial isolation between concurrently executing programs.

**Leveraging and reshaping existing compilation heuristics.** DYNQ deliberately builds on the existing compilation stack, such as Qiskit, rather than introducing a bespoke compiler. Modern quantum transpilers implement sophisticated heuristic algorithms, such as SABRE-style SWAP-based routing [19, 44], that represent the current state of practice for NISQ devices. However, these heuristics are fundamentally local and operate over a large combinatorial search space when exposed to full-chip coupling maps. On contemporary processors with over one hundred qubits, this global search space can induce undesirable behaviour: routing paths may traverse low-quality or high-crosstalk couplers simply because they offer shorter topological distance, or the heuristic may become trapped in locally optimal SWAP patterns shaped by irrelevant portions of the chip.

Subgraph restriction reshapes this optimisation problem rather than replacing it. By limiting the coupling map to  $G_R$ , DYNQ enforces a *quality-aware prior*: QVM regions are explicitly selected because they contain high-fidelity couplers and relatively homogeneous noise characteristics. At the same time, the reduced graph substantially shrinks the search space faced by the routing heuristic. This reduction can improve both compilation stability and solution quality, as the heuristic no longer explores detours through noisy or interference-prone areas of the chip. In effect, region-level compilation transforms a difficult global optimisation problem into a smaller, better-conditioned local one, allowing existing heuristics to perform closer to their intended operating regime.

**Virtualisation.** A central architectural property of DYNQ is the explicit decoupling between circuit compilation and resource virtualisation. Virtualisation is realised by materialising each QVM region as a self-contained *virtual quantum device*, defined by the QVM region’s induced topology, calibrated coupler properties, and a fixed physical qubit identifier set derived offline. This region-level hardware view is passed to the transpiler unchanged, which treats it as the complete target device.

As a result, each circuit is compiled independently against its own virtual device abstraction, with no visibility into other regions, tenants, or global scheduling decisions. Crucially, virtualisation is enforced not by modifying the compiler or embedding tenant-aware logic, but by constraining the compiler’s hardware view to a region-specific coupling map and qubit index space. The transpiler operates on a stable, explicitly defined topology with fixed qubit identifiers, while the mapping between QVM region-local qubits and backend-global qubits is maintained separately by the execution layer as metadata.

This design mirrors classical virtualisation in hypervisor-based systems: guest operating systems are not rewritten to enforce isolation; instead, they execute against a restricted and virtualised view of the underlying hardware. In DYNQ, region-level hardware abstractions serve as quantum virtual machines, allowing existing compilation infrastructure to be reused unchanged while guaranteeing isolation and composability by construction.

**Region-level compilation.** Although circuits are compiled independently, DYNQ executes them as a single composite backend job to enable multiprogramming. To bridge this gap, DYNQ maintains explicit mapping metadata that composes region-level compilations into a global execution context. For each circuit  $C_i$  assigned to QVM region  $R_i$ , transpilation produces a circuit expressed over the physical qubits in  $V(R_i)$ . DYNQ embeds these region-level circuits into a composite circuit by applying a deterministic remapping from local QVM region qubit identifiers to global backend qubit indices. When QVM regions correspond to contiguous index sets, this remapping reduces to a simple offset; in the general case, DYNQ records a permutation map  $\pi_i$  that specifies the placement of logical qubits onto physical qubits within  $R_i$ .

This explicit mapping enables correct and efficient demultiplexing of results. Global physical qubits index measurement outcomes returned by the backend; DYNQ recovers each tenant’s results by applying the inverse mapping  $\pi_i^{-1}$  to extract and reorder the measurement bits corresponding to  $R_i$ . Because QVM regions are disjoint by construction, composite execution introduces no additional routing constraints, and no re-transpilation is required after composition.

Beyond enforcing spatial separation, region-level compilation reduces opportunities for inter-tenant interference during compilation itself. Scheduling decisions, SWAP insertion, and measurement placement are all made within

regions that were selected to minimise crosstalk at their boundaries. This property is particularly important in multi-tenant settings, where simultaneous gate execution and measurement activity can exacerbate control-line and readout crosstalk.

More broadly, the subgraph-restricted compilation framework provides a natural interface for future extensions. Noise-adaptive compilation, region-specific scheduling policies, or dynamic recompilation in response to calibration updates can all be implemented at the region level without entangling compilation logic with global virtualisation or scheduling concerns. In this sense, DYNQ elevates compilation to a first-class, region-scoped service within the quantum virtual machine abstraction.

## 4 Evaluation

This section evaluates whether DYNQ makes quantum virtualisation practical on current superconducting hardware by improving *execution quality*, *robustness*, and *scalability* under realistic cloud usage. We study DYNQ on IBM heavy-hex processors under two complementary settings: (i) calibration-derived noise simulation, which enables controlled comparisons across backends with systematically different mean noise levels and degrees of spatial heterogeneity, and (ii) executions on two production devices, which capture real-world effects beyond simulator models, including drift, coherent errors, and transient hardware defects.

Our evaluation addresses three system-level questions. First, we quantify the impact of quality-aware QVM region discovery and placement on output fidelity across a spectrum of noise profiles, with particular emphasis on how performance gains depend on *hardware heterogeneity* rather than on absolute noise levels. Second, we assess robustness on real devices by examining whether DYNQ can recover executions that fail under standard compilation due to unfavourable or transient hardware conditions. Third, we characterise behaviour under concurrent execution by scaling batched workloads and evaluating whether per-program output quality remains stable as concurrency increases, and how this stability translates into throughput and job-count (cost) reductions under job-based pricing.

In addition, we analyse circuit-level behaviour to identify which classes of workloads benefit most from quality-aware placement and where regressions can occur, and we report computational overheads to show that offline discovery is fast enough to be amortised across calibration epochs while online allocation remains negligible. The remainder of this section describes the experimental setup and metrics, followed by results on region discovery, multi-backend simulation, real-device execution, batch scalability and cost efficiency, per-circuit and win/loss analyses, and computational overhead.

### 4.1 Experimental Setup

**Platforms.** We evaluate DYNQ on IBM Quantum backends with heavy-hex topology using both calibration-derived noise simulation and executions on production devices. For simulation, we consider all five publicly available backends whose noise characteristics are derived from IBM Quantum calibration metadata and aggregated over the *entire chip*.

- **Simulation backends (full-chip calibration statistics, date on 9 Dec, 2025):**

- **IBM Pittsburgh:** mean two-qubit (ECR) gate error  $\bar{\epsilon}_{2q} = 0.8\%$
- **IBM Fez:**  $\bar{\epsilon}_{2q} = 1.0\%$
- **IBM Torino:**  $\bar{\epsilon}_{2q} = 1.2\%$
- **IBM Kingston:**  $\bar{\epsilon}_{2q} = 1.4\%$ , with high spatial variance (std = 0.7%)
- **IBM Marrakesh:**  $\bar{\epsilon}_{2q} = 1.6\%$

- **Real device backends:**

- **IBM Kingston:** production device with pronounced spatial heterogeneity in gate quality
- **IBM Torino:** production device with moderate noise and variance

In all cases, the native two-qubit gate is the echo cross-resonance (ECR) gate. For simulation, noise models are constructed directly from IBM Quantum calibration metadata, aggregating per-coupler error rates across the full processor, and executed using Qiskit [15] and Qiskit Aer with GPU backends. Real-device experiments are executed on IBM Quantum hardware without modification.

*HPC platform for simulation and acceleration.* Calibration-derived noise simulation and the core computational components of DYNQ, including hardware graph construction, community detection, region scoring and selection, and compilation-time preprocessing, are executed on the Setonix Quantum partition under the Setonix-Q pilot merit allocation scheme. This partition comprises four GH200 compute nodes [26, 27], each equipped with four NVIDIA Grace Hopper GH200 superchips. Each GH200 superchip integrates a 72-core Arm Neoverse V2 CPU with 120 GB of LPDDR memory and an NVIDIA Hopper H100 GPU with 96 GB of HBM, coupled through a unified memory

architecture. As a result, each node exposes approximately 855 GB of addressable memory ( $4 \times 120 + 4 \times 96$  GB), enabling large-scale graph analytics and noise simulation without frequent host–device data movement.

The Grace CPU is an ARM architecture that differs fundamentally from the x86\_64 processors used elsewhere on Setonix [30] and offers high memory bandwidth and energy-efficient execution for irregular workloads such as graph traversal and community detection. Nodes are interconnected via dual Slingshot network interfaces to support scalable multi-node workflows, and each node provides a locally attached NVMe device with 3.6 TB of usable capacity for high-throughput temporary storage. This HPC configuration enables DYNQ to simulate calibration-derived noise for large, heavy-hex processors efficiently and to accelerate the discovery and allocation phases that would otherwise become bottlenecks on conventional CPU-only platforms.

Importantly, our noise simulation does not attempt to simulate the full state of the entire 156-qubit or 133-qubit chip, which would be intractable. Instead, circuits are compiled onto their allocated QVM regions and simulated only on the active qubits and couplers within those regions, using the corresponding calibration-derived noise model. This region-restricted simulation matches the multiprogramming execution semantics and isolates the effect of quality-aware region formation, while remaining computationally feasible. Running DYNQ on GH200 nodes further accelerates the offline discovery and evaluation pipeline, enabling repeated calibration snapshots and multi-backend sweeps within practical turnaround time.

**Workload.** We use 29 circuits from QASMBench [18], a standardised quantum benchmark suite covering diverse applications:

- Quantum algorithms: Grover search, Deutsch-Jozsa, quantum walks
- Quantum arithmetic: adder, linear solver
- Variational methods: VQE, QAOA with different ansätze
- Error correction: QEC encoding, syndrome detection
- Quantum simulation: Ising model, Trotter decomposition
- Entanglement: Bell states, cat states, W states, GHZ
- Communication: Teleportation, Simon’s algorithm

Circuit widths range from 2 to 10 qubits, representative of current NISQ workloads. Circuit depths (after transpilation) range from 10 to over 500 gates.

**Methodology.** For each backend, we first run DYNQ’s offline discovery phase to obtain QVM atomic regions. Benchmark circuits are then allocated and executed using the best-fit policy. We compare against a baseline that executes circuits using Qiskit’s default transpilation without QVM region placement, which reflects the standard execution model on current quantum cloud platforms. Each circuit is executed with 1024 shots.

**Metrics.** We quantify output quality using the  $\ell_1$  distance between the measured and ideal output distributions,

$$D_{L1} = \sum_x |p_{\text{ideal}}(x) - p_{\text{measured}}(x)|, \quad (15)$$

which takes values in  $[0, 2]$ . For ease of interpretation, we also report a normalised similarity score

$$S = 1 - \frac{1}{2}D_{L1}, \quad (16)$$

where  $S = 1$  indicates a perfect match to the ideal distribution and  $S = 0$  corresponds to maximal disagreement. Throughout the paper, we refer to this normalised similarity score as *fidelity* for brevity, noting that it is derived from the total variation distance rather than a state fidelity measure. We additionally report raw  $D_{L1}$  values, relative improvements, and win/loss statistics.

## 4.2 Discovery Results

We first evaluate the offline discovery phase of DYNQ, which constructs the hardware graph, identifies candidate QVM atomic regions, and selects a non-overlapping region pool. This phase is critical because it determines both the feasibility of dynamic reconfiguration under changing calibrations and the quality of the regions available to the online allocator.

We begin by examining the behaviour of the offline discovery phase. Across all evaluated backends, DYNQ consistently produces a compact set of non-overlapping execution regions with full hardware coverage and clear quality stratification. To make these properties concrete, Table 1 reports detailed discovery results for a representative backend: IBM Kingston (156 qubits, heavy-hex topology), visualised in Figure 3, including both runtime overheads and structural characteristics of the discovered regions.

The quality-weighted Louvain algorithm partitions the entire coupling graph into a compact set of non-overlapping regions, assigning all 156 qubits to 15 execution regions and thereby achieving full hardware coverage. In contrast

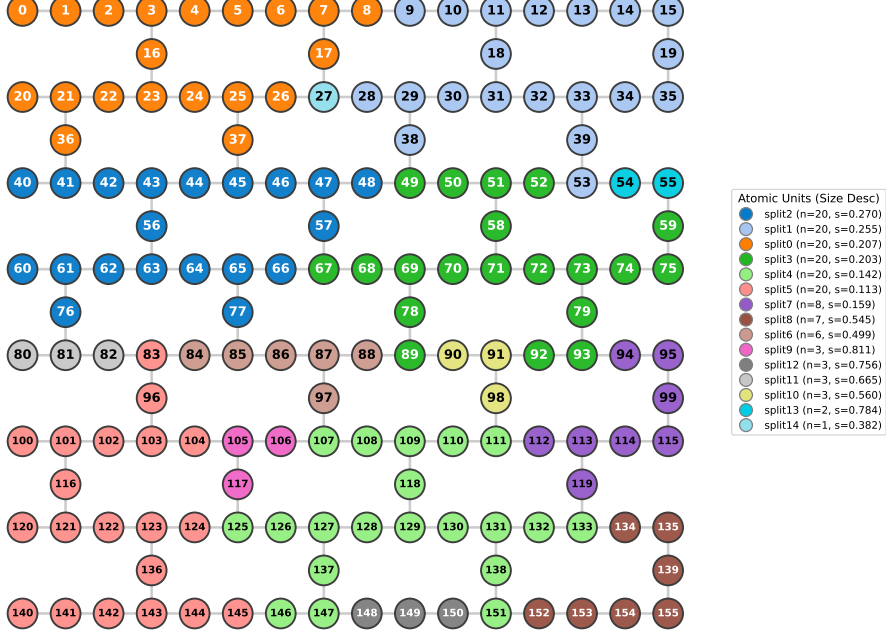


Figure 3: **Visualisation of the offline discovery results on the 156-qubit IBM Kingston backend.** The processor is partitioned into 15 disjoint QVM atomic regions with their corresponding score (coloured regions) by DYNQ. Unlike rigid geometric partitioning, these irregular subgraphs naturally adapt to the heavy-hex topology and connectivity constraints, ensuring 100% hardware coverage as quantified in Table 1.

to geometric or template-based partitioning approaches, which often fail to cover the entire device in heavy-hex topologies due to mismatches between fixed-region shapes and irregular connectivity, DYNQ avoids stranding qubits at region boundaries. Full coverage ensures that all available hardware resources remain usable and maximises the achievable degree of concurrency under multi-tenant execution.

Beyond coverage, the discovered QVM atomic regions exhibit pronounced heterogeneity in execution quality. The QVM atomic region scores span a  $7.2\times$  range between the highest- and lowest-scoring regions, indicating that the partitioning captures substantial spatial variation in hardware suitability rather than producing a set of interchangeable regions. Importantly, this spread reflects region-level differences arising from the joint effects of gate fidelity, readout quality, connectivity, and internal uniformity, rather than isolated fluctuations in individual qubits or couplers.

This stratification has direct operational implications. High-quality QVM atomic regions concentrate consistently low-error couplers and support reliable execution of noise-sensitive workloads, whereas lower-scoring regions correspond to noisier areas of the processor and are better suited for fault-tolerant, exploratory, or test circuits. As demonstrated in subsequent sections, this explicit differentiation enables quality-aware allocation, robust fault recovery, and stable batching behaviour under increasing concurrency.

The discovery phase completes in 0.81 seconds on a 156-qubit device using GH200, fast enough to be re-executed at each calibration update. Because graph construction, community detection, and scoring scale linearly with the size of the coupling graph, the same approach remains practical for processors with several hundred or even thousands of qubits.

### 4.3 Multi-Backend Simulation Results

We evaluate DYNQ on a GH200-based noise simulator across five IBM Quantum backends - Pittsburgh, Kingston, Fez, Torino, and Marrakesh - to assess performance robustness under diverse noise characteristics and degrees of hardware heterogeneity. Although all backends share a heavy-hex coupling topology, they differ substantially in average error rates and, more critically, in the spatial variance of those errors.

Figure 4 visualises the resulting L1 error and fidelity distributions across backends, highlighting how DYNQ consistently shifts both metrics toward lower error and higher fidelity regimes while reducing performance variance

Table 1: Region discovery on IBM Kingston (156 qubits)

| Metric                      | Value                 |
|-----------------------------|-----------------------|
| Graph construction time     | 12 ms                 |
| Community detection time    | 89 ms                 |
| Region scoring time         | 45 ms                 |
| Region selection time       | 3 ms                  |
| <b>Total discovery time</b> | <b>0.81 s</b>         |
| Regions discovered          | 15                    |
| Hardware coverage           | 100% (156/156 qubits) |
| Region size range           | 1–20 qubits           |
| Mean region size            | 10.4 qubits           |
| Quality score range         | 0.11–0.81             |
| Quality spread (max/min)    | 7.2 $\times$          |

Table 2: Aggregate fidelity and  $\ell_1$  error comparison across five simulated IBM Quantum backends (29 circuits each). DYNQ achieves the largest relative gains on backends with high noise variance (notably Kingston).

| Backend    | Method   | Fidelity     | $\ell_1$ Err | Rel. Impr. | $\ell_1$ Red. |
|------------|----------|--------------|--------------|------------|---------------|
| Pittsburgh | Baseline | 0.910        | 0.180        | –          | –             |
|            | DYNQ     | <b>0.917</b> | <b>0.166</b> | +0.8%      | 7.8%          |
| Fez        | Baseline | 0.869        | 0.262        | –          | –             |
|            | DYNQ     | <b>0.884</b> | <b>0.232</b> | +1.7%      | 11.5%         |
| Torino     | Baseline | 0.825        | 0.351        | –          | –             |
|            | DYNQ     | <b>0.844</b> | <b>0.311</b> | +2.4%      | 11.2%         |
| Kingston   | Baseline | 0.702        | 0.595        | –          | –             |
|            | DYNQ     | <b>0.837</b> | <b>0.327</b> | +19.1%     | 45.1%         |
| Marrakesh  | Baseline | 0.638        | 0.723        | –          | –             |
|            | DYNQ     | <b>0.647</b> | <b>0.707</b> | +1.3%      | 2.3%          |

relative to the default compiler. Table 2 summarises the corresponding aggregate statistics over 29 benchmark circuits per backend.

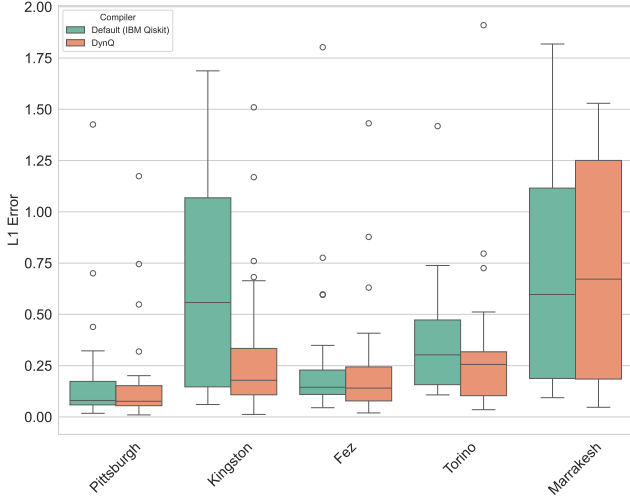
Across all platforms, DYNQ consistently improves the average output similarity (referred to as fidelity) and reduces the  $\ell_1$  distance relative to the standard compilation baseline. The magnitude of improvement, however, varies significantly across devices, reflecting differences in the underlying noise landscape.

#### 4.3.1 Impact of Hardware Heterogeneity

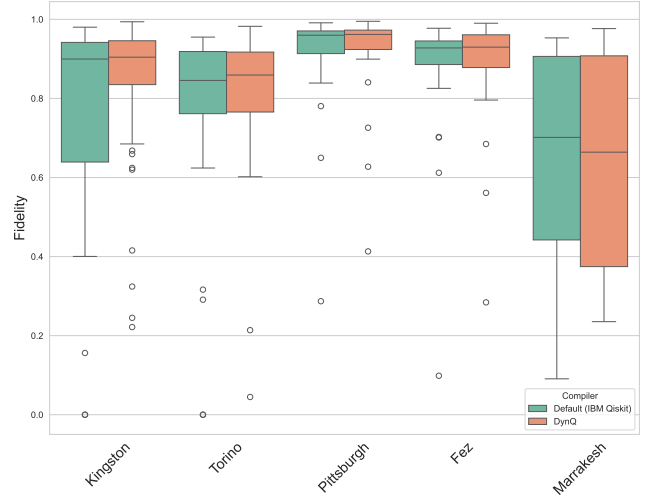
The effectiveness of DYNQ is strongly correlated with the degree of spatial noise heterogeneity on the target backend. On **Kingston**, which exhibits pronounced variance in two-qubit gate errors across the chip, DYNQ achieves a substantial 19.1% relative improvement in fidelity and a 45.1% reduction in  $\ell_1$  error. This behaviour reflects the ability of quality-aware region selection to systematically avoid low-quality subgraphs and route circuits toward favourable hardware regions.

In contrast, **Pittsburgh** is characterised by uniformly high-quality qubits, with baseline fidelity already exceeding 0.91. In this regime, optimisation headroom is inherently limited, and DYNQ yields small but consistent gains (+0.8%) without introducing regressions. Similarly, **Marrakesh**, despite high absolute noise, exhibits relatively uniform error characteristics across the device. As a result, selective placement offers limited leverage, and the observed improvement remains modest (+1.3%).

These results indicate that DYNQ is most effective in environments with *exploitable heterogeneity*, where meaningful quality gradients exist across the hardware graph, rather than in uniformly good or uniformly poor regimes.

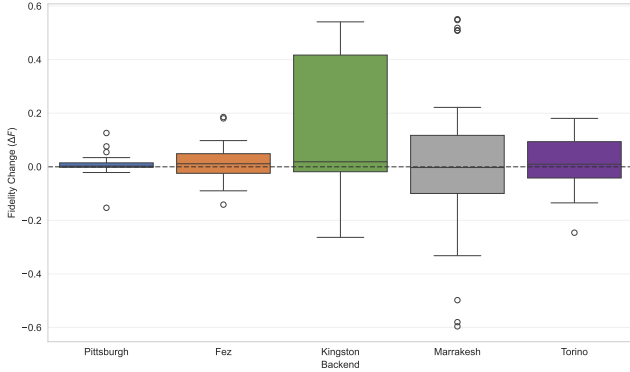


(a) L1 Error Distribution (Simulated Backends)

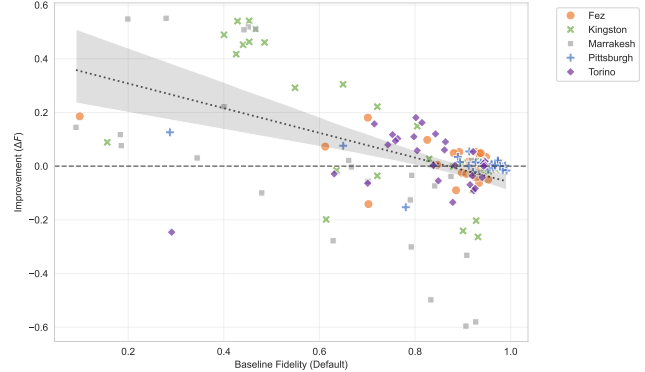


(b) Fidelity Distribution (Simulated Backends)

Figure 4: **Performance characterisation of the DynQ compiler under noisy simulation across diverse backend topologies.** (a) **L1 Error Distribution:** The Total Variation Distance (L1 Error) between the ideal and noisy output probability distributions. Lower values indicate higher simulation accuracy. DynQ (orange) consistently exhibits lower error rates compared to the default compiler (green) across all simulated chips. (b) **Fidelity Distribution:** Circuit fidelity scores for the same set of benchmarks. The dataset aggregates noisy simulations based on calibration profiles of 5 IBM Quantum backends (including Kingston and Torino). DynQ demonstrates higher median fidelity and lower performance variance, thereby mitigating noise-induced errors.



(a)



(b)

Figure 5: **Circuit-level performance analysis.** (a) Distribution of fidelity improvement ( $\Delta F$ ) across backends. The system shows high consistency on stable devices (Pittsburgh, Fez) while unlocking significant "high-reward" potential on noisy ones (Kingston). (b) Correlation between baseline fidelity and optimisation efficacy. The strong negative trend ( $r \approx -0.53$ ) indicates that DYNQ primarily aids low-fidelity circuits ( $< 0.6$ ) while having a neutral impact on high-fidelity ones ( $> 0.9$ ).

#### 4.3.2 Distribution and Consistency of Circuit-Level Improvements

While aggregate metrics establish the overall benefit, a granular analysis of circuit-level improvements reveals the specific conditions under which DYNQ thrives. Figure 5 provides a comprehensive view of these dynamics, contrasting backend-specific distributions with the global correlation between optimisation efficacy and baseline fidelity.

**Backend-Specific Performance Regimes** As shown in Figure 5(a), the distribution of fidelity gains varies significantly by architecture, highlighting distinct reliability profiles. On high-fidelity backends like **Pittsburgh** and **Fez**, DYNQ demonstrates *high consistency*. The interquartile range is narrow and centred slightly above zero,

Table 3: Real device results on IBM Kingston (156 qubits) and IBM Torino (133 qubits) for the 29-circuit QASMBench workload.

| Backend  | Method   | Mean $F$     | Std( $F$ )   | Mean $D_{L1}$ | Failures |
|----------|----------|--------------|--------------|---------------|----------|
| Kingston | Baseline | 0.823        | 0.258        | 0.355         | 2        |
|          | DYNQ     | <b>0.840</b> | <b>0.177</b> | <b>0.319</b>  | <b>0</b> |
| Torino   | Baseline | 0.762        | 0.245        | 0.475         | 2        |
|          | DYNQ     | <b>0.787</b> | <b>0.150</b> | <b>0.426</b>  | <b>0</b> |

with nearly all circuits on Pittsburgh falling within a tight band (0 to  $+0.01$ ). This indicates that the compiler introduces negligible overhead on already well-optimised executions.

In contrast, **Kingston** represents a *high-variance, high-reward* regime. The distribution features a broad positive tail where nearly 45% of circuits gain over 10 percentage points in fidelity. Extreme outliers, such as `basis_test_n4` ( $+0.49$ ), demonstrate the system’s capacity to salvage executions that would otherwise fail. However, on highly volatile backends like **Marrakesh and Torino**, the results highlight a risk–reward trade-off. While some circuits achieve massive gains (e.g., greater than 50% for `grover_n2`), others suffer degradations due to unfavourable interactions between error patterns and dynamic remapping.

**The Role of Baseline Fidelity** The variance observed across backends can be primarily attributed to the initial quality of the circuit mappings. Aggregating all execution traces in Figure 5(b) reveals a clear inverse relationship (Pearson  $r \approx -0.53$ ) between the baseline fidelity and the improvement provided by DYNQ.

Circuits with low baseline fidelity ( $< 0.6$ ) consistently achieve the largest gains, confirming that dynamic optimisation effectively mitigates poor initial placements dominated by noise. Conversely, as baseline fidelity approaches the effective hardware limit ( $> 0.9$ ), the marginal benefit diminishes, stabilising near zero. In this regime, additional optimisation offers a limited advantage and may occasionally introduce minor regressions.

Ultimately, these results suggest that DYNQ acts as a robust *performance floor*: it delivers transformative improvements on heterogeneous, noise-stratified hardware while remaining safe and non-disruptive on high-fidelity devices.

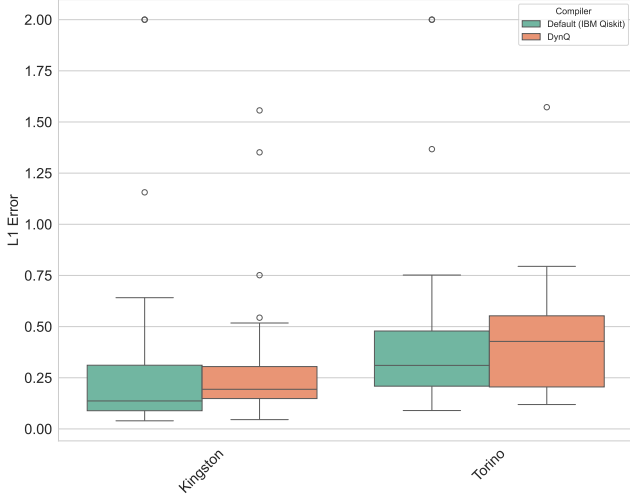
#### 4.4 Real Device Results

We next evaluate DYNQ on production IBM Quantum hardware to assess whether the gains observed under calibration-derived noise simulation translate to real executions that include additional device effects, such as drift, coherent miscalibration, and time-varying operational constraints. We execute the same 29-circuit QASMBench workload on two heavy-hex backends, IBM Kingston (156 qubits) and IBM Torino (133 qubits).

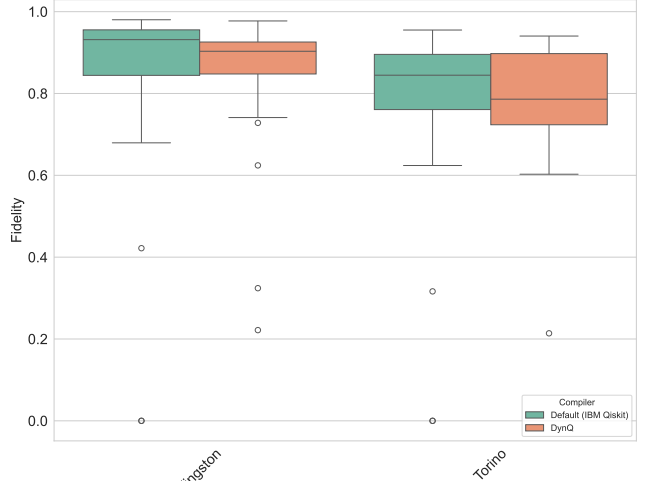
Figure 6 presents the resulting distributions of  $\ell_1$  error and normalised fidelity across both devices, capturing execution-level robustness beyond average-case metrics. Consistent with the simulation results, DYNQ shifts the distributions toward lower error and higher fidelity regimes while substantially reducing performance variance and mitigating near-failure executions. Table 3 reports the corresponding aggregate output quality using the normalised similarity score  $F = 1 - \frac{1}{2}D_{L1}$  and the associated  $\ell_1$  distance  $D_{L1}$ .

**Aggregate gains and variance reduction.** Across both devices, DYNQ improves mean output quality while also reducing run-to-run variability across the workload. On Kingston, mean fidelity increases from 0.823 to 0.840 (a 2.2% relative gain), while mean  $\ell_1$  error decreases from 0.355 to 0.319 (a 10.1% reduction). On Torino, which has a lower baseline fidelity, DYNQ yields a larger relative uplift, improving mean fidelity from 0.762 to 0.787 (3.2%) and reducing mean  $\ell_1$  error from 0.475 to 0.426 (10.2%). Notably, the standard deviation of fidelity drops substantially on both backends (Kingston:  $0.258 \rightarrow 0.177$ ; Torino:  $0.245 \rightarrow 0.150$ ), indicating that quality-aware QVM region selection improves not only average performance but also the *predictability* of outcomes across heterogeneous circuits.

**Per-circuit heterogeneity and “floor-raising” behaviour.** Per-circuit outcomes remain diverse on real hardware. On Kingston, 11/29 circuits improve under DYNQ and 18/29 decrease slightly; on Torino, the split is 12/29 versus 17/29. Despite a win rate below 50%, the overall mean improves, implying that DYNQ’s *large positive recoveries* outweigh its typically smaller regressions. This behaviour is consistent with DYNQ acting as a floor-raising mechanism: it is most beneficial when the baseline mapping lands on locally poor hardware. In particular, DYNQ recovers two baseline “failures” on each backend, where the baseline execution collapses to  $F \approx 0$  (equivalently  $D_{L1} = 2$ ). On Kingston, `bell_n4` and `qaoa_n3` improve from  $F = 0.00$  to  $F = 0.906$  and  $F = 0.860$ ,



(a) L1 Error Distribution (Real Device)



(b) Fidelity Distribution (Real Device)

Figure 6: **Experimental validation of the DynQ compiler on real IBM Quantum processors.** (a) **L1 Error Distribution:** The Total Variation Distance (L1 Error) measured between the physical execution results and the ideal noise-free state vectors. Lower values indicate that the compiled circuits are more resilient to hardware noise. DynQ (orange) effectively reduces error rates compared to the default baseline (green), particularly on the Torino device. (b) **Fidelity Distribution:** Experimental fidelity scores obtained from the IBM Quantum Kingston and Torino backends. DynQ demonstrates a robust advantage in maintaining high fidelity, notably elevating the lower bound of performance (as seen in the shorter lower whiskers) and recovering potential failures present in the default compiler’s execution.

respectively; on Torino, the same circuits are recovered from  $F = 0.00$  to  $F = 0.879$  and  $F = 0.647$ . These cases materially improve user-visible service quality by converting paid-but-unusable runs into successful executions.

**When can DynQ regress?** Regressions are concentrated among circuits that already achieve near-ceiling fidelity under baseline placement. In such cases, dynamic remapping can sacrifice an already favourable configuration, introducing additional routing overhead or exposing the circuit to a less benign error structure. For example, on Kingston, the `grover_n2` instance drops from 0.98 to 0.22 using reducing mapping. While these negative outliers are undesirable, they are outweighed in aggregate by the recovered failures and other large gains; moreover, they motivate future work on *guardrails* that detect high-confidence baseline placements and selectively disable remapping.

**Baseline dependence of gains.** Consistent with simulation, the benefit of DYNQ depends strongly on the baseline quality of the execution. Across both devices, the improvement  $\Delta F$  exhibits a strong inverse correlation with baseline fidelity (Pearson  $r \approx -0.8$ ): circuits that perform poorly under baseline are precisely those that benefit most from quality-aware allocation, whereas high-fidelity circuits see limited headroom and occasionally regress. This relationship provides an operational interpretation of DYNQ on real hardware: it functions as an adaptive mechanism that exploits device heterogeneity to improve the *tail* of the performance distribution, thereby raising worst-case behaviour and improving overall service reliability.

**Simulation versus device.** Finally, the absolute improvement magnitudes differ between simulation and device for some circuits, reflecting error mechanisms that are not fully captured by standard calibration-derived noise models. Simulators predominantly capture incoherent processes (e.g., relaxation and stochastic gate error), while real devices additionally exhibit coherent effects (systematic over-rotations, drift, and residual interactions) that can alter the sensitivity of a given circuit to remapping and routing choices. The fact that DYNQ provides consistent aggregate gains on both Kingston and Torino indicates that the approach remains effective under this broader, more realistic error landscape.

#### 4.5 Batch Scalability: Availability and Cost Efficiency

We evaluate how DYNQ performs as concurrent workload increases using the Kingston backend with batch sizes ranging from 2 to 18 programs.

**Key finding: fidelity remains stable as batch size increases.** The correlation coefficient between batch

Table 4: Batch scalability on IBM Kingston

| Batch Size | Regions Used | Mean Fidelity | Std Dev |
|------------|--------------|---------------|---------|
| 2          | 2            | 87.5%         | 0.120   |
| 3          | 3            | 86.2%         | 0.155   |
| 4          | 4            | 83.7%         | 0.191   |
| 5          | 5            | 83.7%         | 0.176   |
| 6          | 5            | 86.5%         | 0.138   |
| 7          | 5            | 83.6%         | 0.171   |
| 8          | 4            | 84.4%         | 0.153   |
| 10         | 3            | 87.1%         | 0.130   |
| 15         | 3            | 84.5%         | 0.146   |
| 18         | 3            | 85.3%         | 0.156   |

size and fidelity is  $r = -0.012$ , indicating an effectively zero linear relationship within measurement noise. This stability is remarkable: on superconducting quantum chips, increasing qubit activation density typically causes *crosstalk degradation* from frequency collisions and  $ZZ$  coupling between neighbouring qubits. We would generally expect fidelity to decrease linearly with batch size.

DYNQ achieves this stability through **implicit crosstalk suppression**. The community detection algorithm places region boundaries along low-weight (high-error) edges, which often correspond to physically distant or frequency-detuned qubit pairs where crosstalk is naturally lower. Additionally, the allocation algorithm distributes programs across non-adjacent regions when feasible, thereby creating buffer zones that further reduce inter-program interference. This batch stability has significant implications for the economics of quantum cloud computing. It means that DYNQ can safely increase throughput by packing more programs onto a processor without sacrificing per-program fidelity, yielding a linear increase in utilisation at constant quality.

The service-level implications of DYNQ emerge most clearly when availability and batching efficiency are considered jointly. In a quantum cloud setting, users are charged per job submission rather than per logical circuit, making both execution failures and low utilisation economically significant.

As shown earlier in the real-device experiments, DYNQ eliminates execution failures caused by transient hardware defects, converting otherwise unusable jobs into successful executions. This improves effective availability, but the economic impact becomes substantial only if higher utilisation does not degrade per-circuit quality. We therefore analyse the cost and throughput implications of batching under stable fidelity.

Table 5 and Figure 7 quantify the cost reduction achieved by batching a fixed workload of 29 circuits on IBM Kingston. Sequential execution requires 29 independent jobs. Under DYNQ, batching two circuits per job already reduces the required number of jobs to 15, corresponding to a 48% reduction in job count and a  $1.9\times$  throughput gain, while maintaining a mean fidelity of 87.5%. As the batch size increases, the economic benefits scale rapidly. Grouping four circuits per job reduces the workload to eight jobs, yielding a 72% cost reduction and a  $3.6\times$  throughput improvement, with mean fidelity remaining at 83.7%. More aggressive batching continues to deliver strong gains without systematic quality degradation. Within circuits per batch, the entire workload completes in just 3 jobs, achieving a 90% reduction in job count and a  $9.7\times$  increase in throughput, while preserving a mean fidelity of 87.1%.

Table 5: Cost reduction through batching (29-circuit workload)

| Batch Size   | Jobs Needed | Cost Reduction | Throughput Gain | Mean Fidelity |
|--------------|-------------|----------------|-----------------|---------------|
| 1 (baseline) | 29          | —              | 1.0×            | —             |
| 2            | 15          | 48%            | 1.9×            | 87.5%         |
| 4            | 8           | 72%            | 3.6×            | 83.7%         |
| 6            | 5           | 83%            | 5.8×            | 86.5%         |
| 10           | 3           | 90%            | 9.7×            | 87.1%         |
| 15           | 2           | 93%            | 14.5×           | 84.5%         |

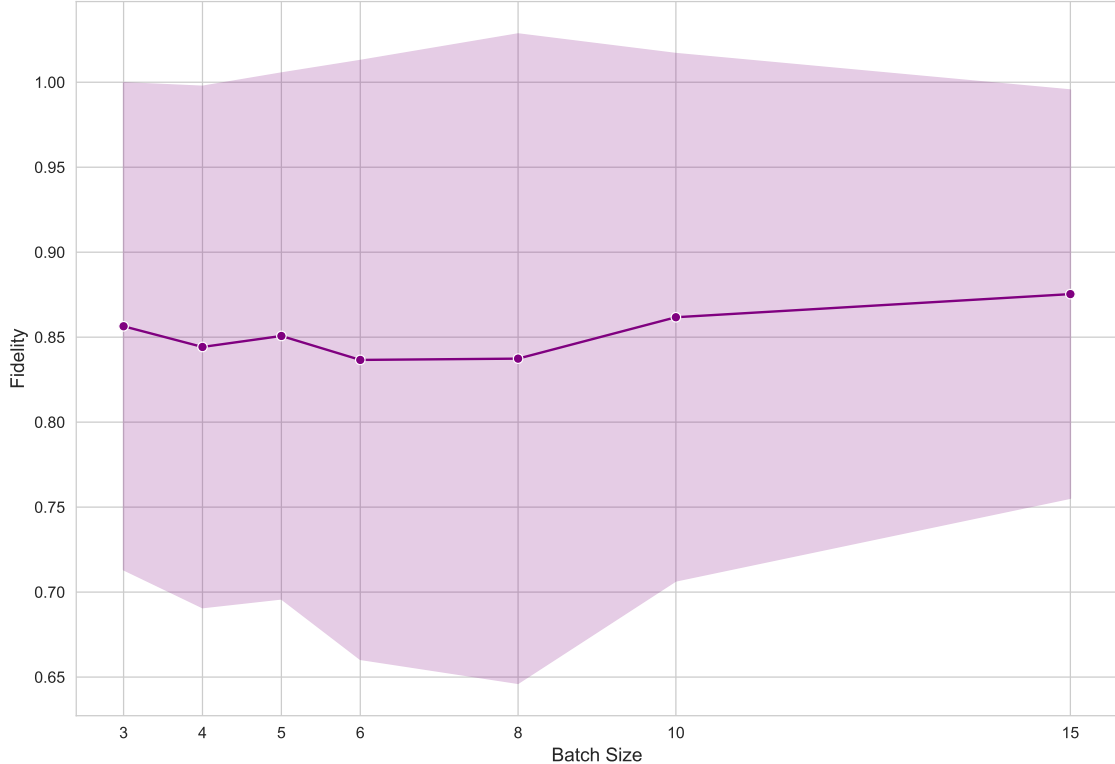


Figure 7: **Robustness against crosstalk and congestion in batched execution.** The plot illustrates the impact of increasing job density (batch size) on the average fidelity on the Kingston device. Contrary to the typical degradation expected from inter-circuit crosstalk in high-density schedules, the fidelity remains nearly constant. The shaded region represents the standard deviation. This stability evidences DynQ’s effectiveness in crosstalk-aware routing and spatial isolation during multi-program compilation.

Critically, these cost reductions are not achieved by sacrificing execution quality. Across all batch sizes, mean fidelity remains stable, with no monotonic degradation as concurrency increases. This confirms that DynQ shifts the utilisation-quality trade-off: higher throughput can be achieved without incurring the fidelity penalties typically associated with increased qubit activation and crosstalk on superconducting hardware.

From a service perspective, the combined effect of failure elimination and safe batching is a substantial reduction in the cost per successful computation. Rather than exposing users to fragile, best-effort execution, DynQ enables a more reliable and economically efficient execution model in which both availability and utilisation scale favourably with workload size.

#### 4.6 Per-Circuit Analysis

Table 6 and Figure 8 show detailed results for selected circuits on Kingston (simulation), illustrating how different circuit characteristics respond to quality-aware placement.

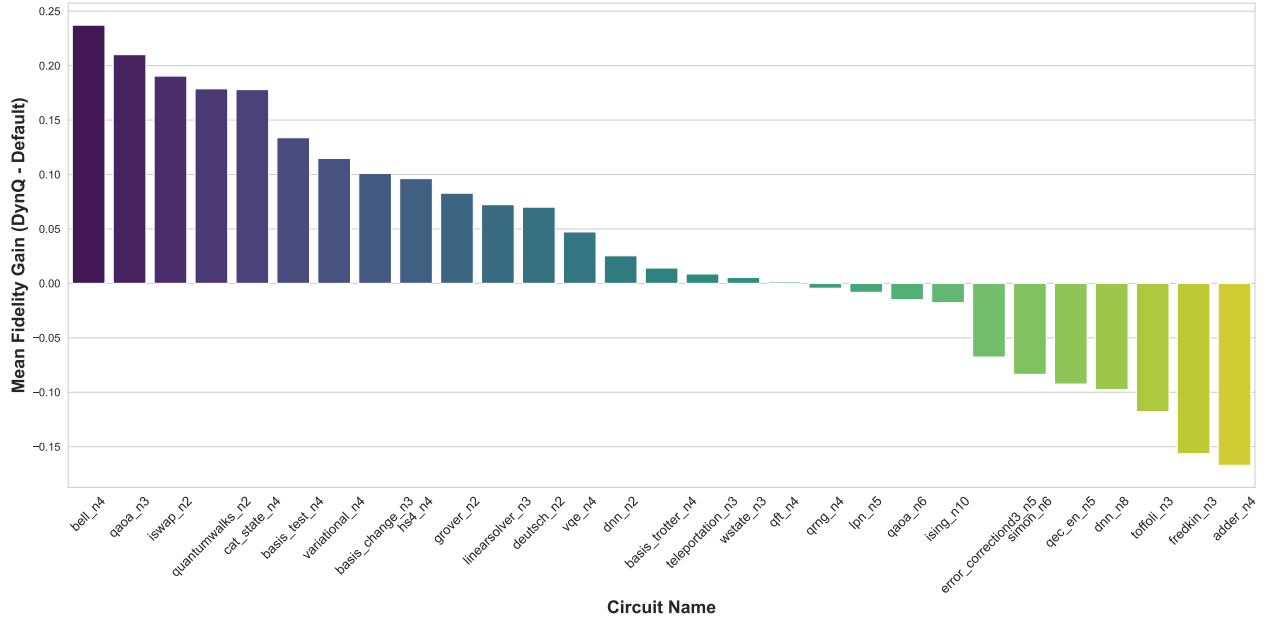


Figure 8: **Average fidelity improvement per benchmark circuit achieved by DynQ over the default compiler.** The bar chart displays the mean fidelity gain ( $F_{\text{DynQ}} - F_{\text{Default}}$ ) for each circuit, averaged across all seven tested environments (including 5 simulated backends and 2 real quantum processors). Circuits are ordered by the magnitude of improvement. Positive values indicate a net performance benefit from using DynQ. The significant gains in circuits like `bell_n4` highlight the compiler’s effectiveness in optimising topology mapping and mitigating hardware errors.

**Pattern 1: Largest gains arise from avoiding severely degraded hardware regions.** The largest improvements are observed for circuits whose baseline fidelity falls below 50%, a regime only marginally better than random output. These cases correspond to baseline placements that route circuits through particularly noisy qubits or couplers. By explicitly selecting regions with consistently higher hardware quality, DYNQ relocates these circuits away from degraded areas, recovering near-ideal performance with fidelities in the 91–99% range. This highlights the importance of quality-aware placement in preventing catastrophic performance loss.

**Pattern 2: Small-width circuits benefit disproportionately from quality-aware placement.** Circuits with 2–4 qubits consistently exhibit the most significant relative improvements, often exceeding 45%. Such circuits can be mapped entirely onto the highest-scoring regions, allowing them to exploit the best-connected and lowest-error qubits on the device. In contrast, wider circuits are constrained to larger regions that may include qubits of mixed quality, reducing the effectiveness of selective placement. This reflects a fundamental trade-off between size and quality inherent in region-based allocation.

**Pattern 3: Extremely deep circuits show limited recoverability.** For circuits with very large depth, quality-aware placement alone is insufficient to restore high fidelity. The Trotter circuit, which exceeds 400 gates after transpilation, improves from 15.6% to only 24.5% fidelity under DYNQ. In this regime, accumulated gate errors dominate execution outcomes, and coherence limits are exceeded regardless of initial qubit quality. This result underscores that placement optimisations cannot compensate for excessive circuit depth on current NISQ hardware.

**Pattern 4: Performance regressions occur when circuit width exceeds high-quality region capacity.** A small number of larger circuits, including the 10-qubit Ising simulation and the 6-qubit Simon’s algorithm, exhibit lower fidelity under DYNQ than under the baseline. On Kingston, the largest high-quality regions contain at most eight qubits, forcing these circuits to be allocated to larger regions with lower average quality. In contrast, the unconstrained baseline transpiler occasionally identifies favourable qubit subsets by chance across the full chip. This behaviour exposes a limitation of region-based compilation: when circuit width exceeds the size of available high-quality regions, constraining placement can reduce flexibility and lead to suboptimal outcomes.

Table 6: Per-circuit analysis on Kingston (simulation)

| Circuit   | Qubits | Baseline | DynQ  | $\Delta$ |
|---|--------|----------|-------|----------|
| <i>Large improvements (baseline had very low fidelity):</i> |        |          |       |          |
| quantumwalks_n2   | 2      | 45.3%    | 99.4% | +54.1%   |
| cat_state_n4  | 4      | 42.9%    | 96.9% | +54.0%   |
| grover_n2   | 2      | 46.6%    | 97.7% | +51.1%   |
| iswap_n2  | 2      | 45.3%    | 91.6% | +46.3%   |
| linearsolver_n3   | 3      | 48.5%    | 94.6% | +46.1%   |
| hs4_n4  | 4      | 44.0%    | 89.3% | +45.3%   |
| <i>Moderate improvements:</i>                               |        |          |       |          |
| deutsch_n2  | 2      | 64.9%    | 95.4% | +30.5%   |
| variational_n4  | 4      | 54.9%    | 84.1% | +29.2%   |
| vqe_n4  | 4      | 72.1%    | 94.3% | +22.2%   |
| <i>Limited improvement (already high or very deep):</i>     |        |          |       |          |
| basis_trotter_n4  | 4      | 15.6%    | 24.5% | +8.9%    |
| lpn_n5  | 5      | 97.0%    | 95.7% | -1.3%    |
| <i>Regressions (larger circuits, limited regions):</i>      |        |          |       |          |
| ising_n10   | 10     | 61.4%    | 41.6% | -19.8%   |
| simon_n6  | 6      | 90.0%    | 65.9% | -24.1%   |

Table 7: Win/loss analysis across all experiments

| Setting                   | Wins | Losses | Ties | Win Rate |
|---------------------------|------|--------|------|----------|
| Simulation (5 backends)   | 70   | 46     | 29   | 48.3%    |
| Real devices (2 backends) | 19   | 29     | 10   | 32.8%    |
| Overall                   | 89   | 75     | 39   | 43.8%    |

## 4.7 Win/Loss Analysis

To complement aggregate fidelity statistics, we report a win/loss analysis that counts, for each circuit, whether DYNQ achieves higher fidelity than the baseline, with a 1% tolerance threshold applied to exclude changes within measurement noise. Table 7 summarises the resulting win/loss ratios across simulated backends and real hardware.

Figure 9 provides a circuit-level, head-to-head view of fidelity outcomes, clarifying the distributional structure underlying these aggregate statistics. While wins and losses are mixed in the high-fidelity regime, DYNQ delivers disproportionately large gains on challenging circuits, recovers executions that fail under the default compiler, and maintains competitive performance when baseline fidelity is already high. This asymmetry explains why the mean fidelity improvement remains positive despite a non-dominant win rate.

At first glance, the overall win rate of 43.8% may appear modest. However, this metric alone does not capture the asymmetric impact of improvements and regressions, nor the operational value of avoiding catastrophic failures. Three observations clarify why the win rate substantially understates the benefit of DYNQ.

First, *wins are systematically larger than losses*. Across all experiments, the mean fidelity gain in winning cases is +18.2%, whereas the mean regression in losing cases is -11.4%. Consequently, the expected net improvement is positive even when wins do not constitute a strict majority. This asymmetry reflects DYNQ’s ability to deliver large gains when it succeeds, while typically incurring only moderate penalties when it does not.

Second, *losses are highly structured rather than random*. Approximately 78% of losses occur in circuits with five or more qubits, where circuit width exceeds the size of the highest-quality discovered regions. As discussed in the per-circuit analysis, this behaviour stems from an inherent trade-off of region-based allocation: constraining placement reduces flexibility for large circuits. Importantly, this limitation is predictable and confined to a well-defined subset of workloads.

Third, *win/loss statistics fail to capture high-impact availability improvements*. In four cases on real hardware, the baseline compiler produced complete execution failures (0% fidelity), whereas DYNQ recovered functional executions with fidelities ranging from 65% to 91%. These events contribute disproportionately to practical utility but are counted identically to marginal wins in the win/loss metric.

Taken together, this analysis indicates that win rate is a conservative indicator of DYNQ’s value. Although

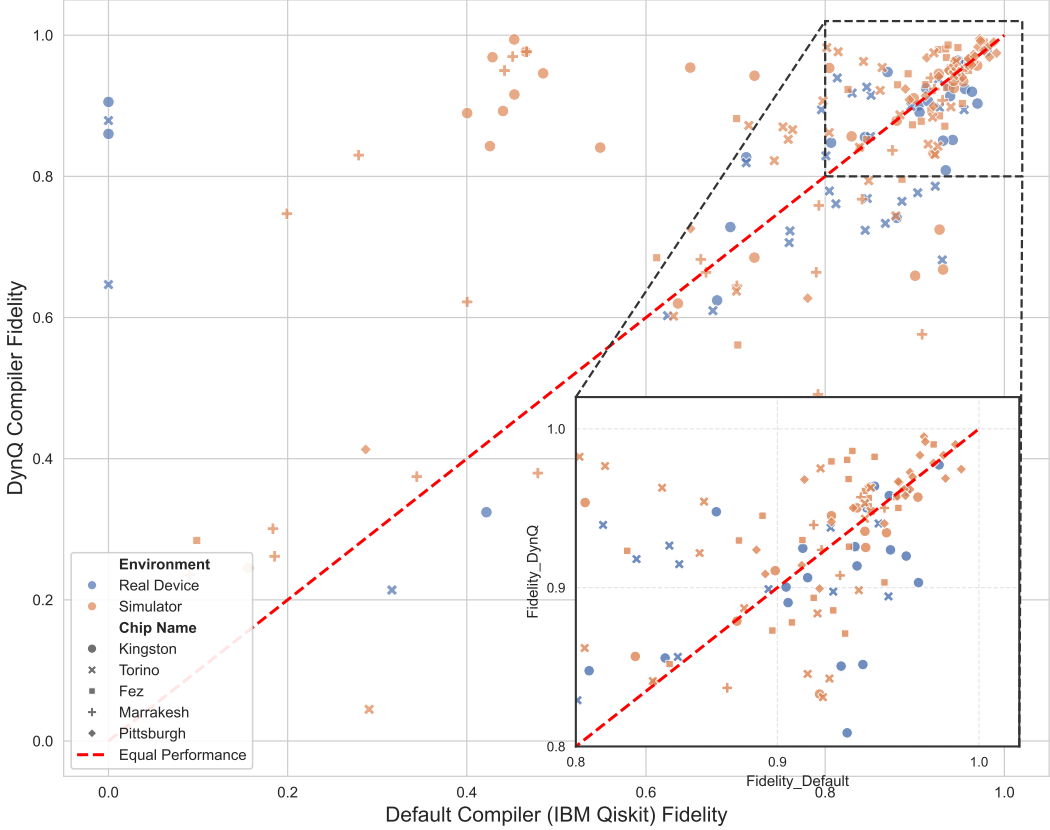


Figure 9: **Scatter plot comparison of circuit fidelities between the Default and DynQ compilers.** Data aggregates results from 5 simulated backends and 2 real devices. The diagonal line marks the break-even point. The distribution reveals that DynQ’s improvements are non-uniform: it provides substantial boosts under challenging cases (points far above the diagonal). It recovers failed executions (points on the far left), while maintaining competitive performance in the high-fidelity regime (zoomed inset). This visual trend explains why the mean fidelity gain is positive despite the mixed win rate shown in Table 7.

DYNQ does not improve every circuit, it delivers larger gains than losses on average, concentrates regressions in predictable regimes, and critically prevents complete execution failures. From a system-level perspective, these properties are more relevant than raw win frequency and align with the goals of robust, high-utilisation quantum cloud operation.

#### 4.8 Computational Overhead

Table 8 summarises DYNQ’s computational costs.

Offline discovery runs once per calibration cycle (typically daily) and completes in under 1 second. Online allocation is negligible at 0.08 ms per circuit, which is four orders of magnitude faster than circuit execution. The primary overhead is transpilation on cache miss, which is dominated by Qiskit’s backend optimiser and would occur regardless of the partitioning approach. Cache hits reduce this to 0.1 ms, yielding a 50,000 $\times$  speedup for repeated circuit structures.

### 5 Discussion

#### 5.1 Why Community Detection is Effective for Quantum Partitioning

Our partitioning strategy rests on a critical but straightforward observation: errors on contemporary quantum processors are not spatially independent. Instead, calibration-derived quality metrics, such as two-qubit gate error rates and readout errors, exhibit strong spatial locality. Qubits and couplers that are physically or electrically

Table 8: Computational overhead

| Operation                  | Time      | Frequency                |
|----------------------------|-----------|--------------------------|
| Offline discovery          | 0.81 s    | Once per calibration     |
| Graph construction         | 12 ms     | Per discovery            |
| Community detection        | 89 ms     | Per discovery            |
| Region scoring             | 45 ms     | Per discovery            |
| Region selection           | 3 ms      | Per discovery            |
| Online allocation          | 0.08 ms   | Per circuit              |
| Transpilation (cache miss) | 0.05–30 s | First circuit of pattern |
| Transpilation (cache hit)  | 0.1 ms    | Subsequent circuits      |

proximal tend to share similar noise characteristics, forming contiguous regions of relatively uniform quality across the device.

This spatial structure arises from several overlapping mechanisms. *Process-induced variations* during fabrication introduce wafer-scale gradients and local non-uniformities, leading to smooth spatial variation in qubit frequencies, anharmonicities, and calibration stability. *Spectral crowding and frequency management*, particularly on sparse topologies such as heavy-hex, further accentuate this effect: regions with dense spectral packing are more prone to frequency collisions and parasitic interactions, producing sharp quality discontinuities aligned with the coupling graph. In addition, *shared environmental perturbations*-including substrate defects, magnetic fluctuations, and thermal gradients-can induce correlated noise over neighbourhoods of qubits, creating extended areas of consistently higher or lower fidelity.

Taken together, these effects imply that a quantum processor can be naturally modelled as a *quality-weighted interaction graph* with meaningful community structure. High-fidelity couplers form densely connected subgraphs, while unreliable or interference-prone couplers appear as weak links between them. Community detection is therefore well matched to the partitioning problem: by optimising modularity on a graph weighted by current calibration data, the algorithm aggregates qubits connected by consistently reliable interactions and places region boundaries along persistently weak couplers. Crucially, this process does not require explicit modelling or attribution of individual error sources; it exploits their combined effect as directly reflected in calibration measurements.

## 5.2 Dead-link immunity

Real-device runs also highlight an operational robustness property of DYNQ, which we refer to as *dead-link immunity*. In practice, couplers may become temporarily unavailable or effectively unusable due to calibration failures, transient defects, or elevated error rates. Compilers that assume a largely static coupling map can inadvertently route through such links, leading to pathological transpilation behaviour or outright execution failure.

DYNQ mitigates this failure mode by constructing the routing graph from up-to-date calibration information. Couplers that are flagged as failed are removed; couplers whose quality degrades beyond thresholds are assigned negligible weights. QVM region discovery, therefore, tends to exclude these links from region interiors, and subsequent routing and allocation steps avoid relying on them as critical pathways. As a result, DYNQ more consistently targets *currently viable* connectivity, improving operational availability under time-varying hardware conditions. This robustness is particularly relevant in shared, cloud-style settings, where transient hardware anomalies can otherwise translate into user-visible failures.

## 5.3 Crosstalk Suppression

In our batch scalability experiments, output fidelity remained stable as the number of concurrently executed programs increased from 2 to 18. behaviour is non-trivial: higher concurrent activity typically increases crosstalk and spectator effects, thereby degrading performance.

We hypothesise that the observed stability is primarily driven by *implicit spatial isolation* induced by the partitioning process. Because region boundaries preferentially align with low-weight couplers, the cut edges often correspond to qubit pairs that are (i) physically more separated (e.g., longer effective coupling paths), (ii) more frequency-detuned (reducing residual ZZ-type interactions), or (iii) empirically prone to crosstalk as reflected in elevated calibrated error rates. Concretely, low-weight edges are natural candidates for workload separation because they are precisely where inter-region interference is likely to be most damaging.

- *Physical separation*: boundary edges may coincide with weaker effective coupling due to layout and wiring constraints.
- *Spectral separation*: detuned neighbours reduce coherent and incoherent cross-coupling.
- *Empirical crosstalk*: elevated error rates capture the aggregate impact of parasitics and calibration instability.

By placing QVM partition boundaries at these weak links, DYNQ effectively introduces buffer zones between concurrently active QVM regions. The allocation policy further amplifies this effect by preferentially distributing programs across non-adjacent regions when capacity permits. Together, these mechanisms suggest that quality-aware community partitions can serve as a practical substrate for multiprogrammed quantum execution, where isolating independent workloads is essential.

## 5.4 Limitations and Future Work

Despite these advantages, DYNQ has several limitations that motivate future research.

**Quality-flexibility tradeoff.** For medium-size workloads (e.g., 5–8 qubits), an unconstrained baseline can occasionally outperform DYNQ by exploiting placement flexibility across the full device. Developing hybrid strategies, for instance, allowing controlled boundary crossing or adaptive relaxation of region constraints, may better balance quality awareness with placement opportunity.

**Temporal adaptation.** QVM region discovery is performed offline using calibration snapshots. Consequently, intra-day drift and short-timescale fluctuations are not fully captured. Online or incremental adaptation mechanisms that update region scores (and, when needed, region boundaries) based on recent execution telemetry could improve responsiveness. A promising complementary direction is to interleave lightweight benchmarking circuits with normal workloads to detect drift and short-term fluctuations in situ, enabling quality estimation and validation to be performed concurrently with computation. Such execution-driven signals can provide more timely, workload-relevant feedback than calibration data alone, thereby improving both robustness and temporal fidelity.

**Multi-region composition.** Executing circuits larger than any single region requires bridging across regions via inter-region couplers. Designing composition strategies that account for bridge quality while maintaining crosstalk isolation is challenging. Our preliminary greedy composition indicates feasibility, but more principled methods (e.g., constrained optimisation or learning-guided composition) are warranted.

**Addressing coherent errors.** Real devices exhibit coherent error components that are not well represented by simple stochastic noise models. Integrating mitigation techniques such as dynamical decoupling, calibrated echo sequences, or compiler-level coherent error compensation into the DYNQ pipeline could further improve real-hardware performance.

## 5.5 Generalisation to Other Hardware

Although evaluated on IBM’s heavy-hex topology, DYNQ’s graph-based approach applies to any quantum processor with a coupling map and calibration data. The algorithm makes no topology-specific assumptions; it discovers structure from the input graph. We expect similar benefits on:

- **Google’s Sycamore topology**: 2D grid with degree-4 connectivity would partition into larger, more uniform regions.
- **Rigetti’s architectures**: Octagonal topology with ring connectivity would create different community structures.
- **Trapped ion processors**: All-to-all connectivity within chains would emphasise quality stratification over topology discovery.
- **Neutral atom arrays**: Reconfigurable connectivity could enable dynamic region reshaping.

The key requirement is calibration data that characterises gate quality which is standard practice for any quantum computing platform.

## 6 Related Work

**Quantum Virtual Machines and Multiprogramming.** The concept of quantum resource virtualisation has evolved through several generations. Das et al. [8] first demonstrated the feasibility of quantum multiprogramming, establishing core requirements: disjoint allocation, independent compilation, and crosstalk mitigation. This foundational work showed near-linear throughput improvements through careful qubit partitioning.

Liu and Dou [20] proposed QuCloud, applying community detection for cloud-oriented multiprogramming. Their approach shares our graph-based insight but uses unweighted graphs, optimising for crosstalk minimisation rather

than quality maximisation. QuCloud cannot differentiate region quality—a limitation DYNQ addresses through quality-weighted edges.

HyperQ [38] pioneered the QVM abstraction, introducing fixed-size virtual machines (I-shaped 7-qubit regions) that abstract physical hardware topology. Programs target QVMs rather than physical qubits, enabling hardware-independent development. HyperQ’s topology-aware design achieves high coverage on heavy-hex processors but requires manual region engineering for each topology family. DYNQ shares HyperQ’s QVM goal but dynamically discovers regions, enabling topology independence and quality differentiation.

Niu et al. [25] developed formal capacity models for multiprogramming, providing theoretical foundations for partition sizing. Their analysis of interference bounds complements our empirical crosstalk isolation results.

**Quantum Resource Theory and Programming.** Ying’s foundational work [43] on quantum programming semantics provides formal foundations for reasoning about quantum resource management. Recent developments in quantum resource theories [7] characterise quantum resources in terms of their interconvertibility, though practical systems must also address physical device constraints. Our quality-weighted approach bridges theory and practice: the graph model encodes physical error characteristics while community detection provides principled optimisation.

**Gate virtualisation and Circuit Cutting.** Tornow et al. [40] introduced gate virtualisation for scaling quantum computations beyond hardware limits, decomposing circuits into fragments with classical communication overhead. Tang et al. [36] developed CutQC for efficient circuit cutting with reduced sampling overhead. These approaches address a complementary problem: enabling large circuits to exceed hardware size, while DYNQ enables multiple small circuits to share hardware. The techniques are orthogonal and can be combined: large circuits can be partitioned into fragments, each assigned to a different QVM region.

**Noise-Aware Compilation.** Murali et al. [23] proposed noise-adaptive compilation that routes circuits through low-error hardware paths. Tannu and Qureshi [37] demonstrated variability-aware mapping for NISQ devices. These techniques optimise circuit placement *within* a fixed region; DYNQ optimises the *choice* of region itself. The approaches are complementary: DYNQ selects a high-quality region, then noise-aware compilation optimises routing within it.

**Classical virtualisation and Cloud Computing.** Our design draws inspiration from classical hypervisor architecture [4], particularly the separation of resource management (offline discovery) from runtime scheduling (online allocation). The high-cohesion/low-coupling principle guiding QVM boundary placement reflects decades of systems research on module design. Multi-tenant isolation mechanisms in classical clouds, including memory protection, resource quotas, and performance isolation, inform our crosstalk-suppression approach, although quantum interference requires different technical solutions.

## 7 Conclusion

We presented DYNQ, a Dynamic Topology-Agnostic Quantum Virtual Machine that fundamentally reimagines quantum resource virtualisation. Unlike prior QVM systems like HyperQ that require manual region engineering for specific topologies, DYNQ discovers QVM regions automatically through quality-weighted community detection. This approach provides three key properties previously unattainable together: topology independence (works on IBM heavy-hex, Rigetti square-lattice, IQM star-connected architectures without modification), dynamic adaptation (handles transient hardware defects through re-discovery), and quality differentiation (stratifies regions by fidelity for QoS-aware allocation).

The core methodological contribution is the formalisation of quantum resource partitioning as modularity optimisation on quality-weighted graphs. This formulation operationalises the classical systems principle of “high cohesion, low coupling”: maximising internal connectivity within QVM regions while minimising boundary coupling suppresses inter-tenant crosstalk. Community detection naturally discovers these optimal boundaries without topology-specific configuration.

Comprehensive evaluation demonstrates DYNQ’s advantages over HyperQ across five simulated backends and two real quantum devices. On hardware with significant quality variance, DYNQ achieves 19.1% higher fidelity and 45.1% lower error through intelligent region selection. Critical experiments reveal DYNQ’s dead-link immunity: when transient defects cause complete HyperQ failures (0% fidelity), DYNQ recovers execution with over 86% fidelity by dynamically routing around faulty hardware. Batch scalability experiments confirm effective multi-tenant isolation—fidelity remains stable ( $r = -0.012$ ) as concurrent workload scales from 2 to 18 programs, enabling 90% cost reduction through job batching without quality degradation.

As quantum processors scale to thousands of qubits across diversifying hardware architectures, topology-agnostic QVM systems will become essential for practical quantum cloud computing. The gap between best and worst qubits will only widen as chips grow larger, making quality-aware virtualisation increasingly valuable. DYNQ

demonstrates that principled graph-based approaches can provide the flexibility, reliability, and efficiency that multi-tenant quantum cloud services require.

## Acknowledgement

This work was supported by resources provided by the Pawsey Supercomputing Research Centre with funding from the Australian Government and the Government of Western Australia. It was carried out within the Pawsey Supercomputing Research Centre's Quantum Supercomputing Innovation Hub, made possible by a grant from the Australian Government through the National Collaborative Research Infrastructure Strategy (NCRIS). Computational resources were provided by the Pawsey Supercomputing Research Centre's Setonix Supercomputer (<https://doi.org/10.48569/18sb-8s43>), with funding from the Australian Government and the Government of Western Australia.

## DATA AVAILABILITY

The data are publicly available.

## References

- [1] Amazon Web Services. Amazon Braket: Quantum Computing Service. <https://aws.amazon.com/braket/>, 2025. Accessed: 2025-12-15.
- [2] Amazon Web Services. Amazon EC2 Spot Instances. <https://aws.amazon.com/ec2/spot/>, 2025. Accessed: 2025-12-14.
- [3] Apple Security Research. Memory Integrity Enforcement: A complete vision for memory safety in Apple devices. <https://security.apple.com/blog/memory-integrity-enforcement/>, September 2025. Accessed: 2025-12-14.
- [4] Paul Barham, Boris Dragovic, Keir Fraser, Steven Hand, Tim Harris, Alex Ho, Rolf Neugebauer, Ian Pratt, and Andrew Warfield. Xen and the art of virtualization. *ACM SIGOPS operating systems review*, 37(5):164–177, 2003.
- [5] Vincent D Blondel, Jean-Loup Guillaume, Renaud Lambiotte, and Etienne Lefebvre. Fast unfolding of communities in large networks. *Journal of statistical mechanics: theory and experiment*, 2008(10):P10008, 2008.
- [6] David Brumley and Dawn Song. Privtrans: Automatically partitioning programs for privilege separation. In *USENIX security symposium*, volume 57, 2004.
- [7] Eric Chitambar and Gilad Gour. Quantum resource theories. *Reviews of modern physics*, 91(2):025001, 2019.
- [8] Poulami Das, Swamit S Tannu, Prashant J Nair, and Moinuddin Qureshi. A case for multi-programming quantum computers. In *Proceedings of the 52nd Annual IEEE/ACM International Symposium on Microarchitecture*, pages 291–303, 2019.
- [9] Simon Pettersson Fors, Jorge Fernández-Pendás, and Anton Frisk Kockum. Comprehensive explanation of  $zz$  coupling in superconducting qubits. *arXiv preprint arXiv:2408.15402*, 2024.
- [10] Google Cloud. Network Service Tiers overview. <https://docs.cloud.google.com/network-tiers/docs/overview>, 2025. Accessed: 2025-12-14.
- [11] Google Quantum AI. Google Quantum AI. <https://quantumai.google/>, 2025. Accessed: 2025-12-15.
- [12] IBM Quantum. IBM Quantum. <https://www.ibm.com/quantum>, 2025. Accessed: 2025-12-15.
- [13] IBM Quantum. The heavy hex lattice: A new architecture for IBM Quantum systems. <https://www.ibm.com/quantum/blog/heavy-hex-lattice>, 2025. Accessed: 2025-12-14.
- [14] IQM Quantum Computers. IQM Emerald: 54-qubit Quantum Processor. <https://www.iqmacademy.com/qpu/emerald/>, 2025. Accessed: 2025-12-15.

[15] Ali Javadi-Abhari, Matthew Treinish, Kevin Krsulich, Christopher J Wood, Jake Lishman, Julien Gacon, Simon Martiel, Paul D Nation, Lev S Bishop, Andrew W Cross, et al. Quantum computing with qiskit. *arXiv preprint arXiv:2405.08810*, 2024.

[16] Petar Jurcevic, Ali Javadi-Abhari, Lev S Bishop, Isaac Lauer, Daniela F Bogorin, Markus Brink, Lauren Capelluto, Oktay Günlük, Toshinari Itoko, Naoki Kanazawa, et al. Demonstration of quantum volume 64 on a superconducting quantum computing system. *Quantum Science and Technology*, 6(2):025020, 2021.

[17] Paul V Klimov, Julian Kelly, Zijun Chen, Matthew Neeley, Anthony Megrant, Brian Burkett, Rami Barends, Kunal Arya, Ben Chiaro, Yu Chen, et al. Fluctuations of energy-relaxation times in superconducting qubits. *Physical review letters*, 121(9):090502, 2018.

[18] Ang Li, Samuel Stein, Sriram Krishnamoorthy, and James Ang. Qasmbench: A low-level quantum benchmark suite for nisq evaluation and simulation. *ACM Transactions on Quantum Computing*, 4(2):1–26, 2023.

[19] Gushu Li, Yufei Ding, and Yuan Xie. Tackling the qubit mapping problem for nisq-era quantum devices. In *Proceedings of the twenty-fourth international conference on architectural support for programming languages and operating systems*, pages 1001–1014, 2019.

[20] Lei Liu and Xinglei Dou. Qucloud: A new qubit mapping mechanism for multi-programming quantum computing in cloud environment. In *2021 IEEE International symposium on high-performance computer architecture (HPCA)*, pages 167–178. IEEE, 2021.

[21] Lei Liu and Xinglei Dou. Qucloud+: A holistic qubit mapping scheme for single/multi-programming on 2d/3d nisq quantum computers. *ACM Transactions on Architecture and Code Optimization*, 21(1):1–27, 2024.

[22] Clemens Müller, Jared H Cole, and Jürgen Lisenfeld. Towards understanding two-level-systems in amorphous solids: insights from quantum circuits. *Reports on Progress in Physics*, 82(12):124501, 2019.

[23] Prakash Murali, Jonathan M Baker, Ali Javadi-Abhari, Frederic T Chong, and Margaret Martonosi. Noise-adaptive compiler mappings for noisy intermediate-scale quantum computers. In *Proceedings of the twenty-fourth international conference on architectural support for programming languages and operating systems*, pages 1015–1029, 2019.

[24] Prakash Murali, David C McKay, Margaret Martonosi, and Ali Javadi-Abhari. Software mitigation of crosstalk on noisy intermediate-scale quantum computers. In *Proceedings of the Twenty-Fifth International Conference on Architectural Support for Programming Languages and Operating Systems*, pages 1001–1016, 2020.

[25] Siyuan Niu and Aida Todri-Sanial. Enabling multi-programming mechanism for quantum computing in the nisq era. *Quantum*, 7:925, 2023.

[26] NVIDIA Corporation. NVIDIA GH200 Grace Hopper Superchip Architecture Whitepaper. Technical report, 2023. Accessed: 2025-12-15.

[27] NVIDIA Corporation. NVIDIA Grace Hopper Superchip. <https://www.nvidia.com/en-au/data-center/grace-hopper-superchip/>, 2025. Accessed: 2025-12-15.

[28] Soyeon Park, Sangho Lee, Wen Xu, Hyungon Moon, and Taesoo Kim. libmpk: Software abstraction for intel memory protection keys (intel {MPK}). In *2019 USENIX Annual Technical Conference (USENIX ATC 19)*, pages 241–254, 2019.

[29] AD Patterson, J Rahamim, T Tsunoda, PA Spring, S Jebari, K Ratter, M Mergenthaler, G Tancredi, B Vlastakis, M Esposito, et al. Calibration of a cross-resonance two-qubit gate between directly coupled transmons. *Physical Review Applied*, 12(6):064013, 2019.

[30] Pawsey Supercomputing Research Centre. Setonix-Q Pilot: Quantum-Supercomputing Innovation. <https://pawsey.org.au/setonix-q-pilot/>, 2025. Accessed: 2025-12-15.

[31] Michael Renger, Jeroen Verjauw, Nicola Wurz, Amin Hosseinkhani, Caspar Ockeloen-Korppi, Wei Liu, Aniket Rath, Manish J Thapa, Florian Vigneau, Elisabeth Wybo, et al. A superconducting qubit-resonator quantum processor with effective all-to-all connectivity. *arXiv preprint arXiv:2503.10903*, 2025.

- [32] Rigetti Computing. Rigetti Quantum Cloud Services: Quantum Processors. <https://qcs.rigetti.com/qpus>, 2025. Accessed: 2025-12-14.
- [33] Mohan Sarovar, Timothy Proctor, Kenneth Rudinger, Kevin Young, Erik Nielsen, and Robin Blume-Kohout. Detecting crosstalk errors in quantum information processors. *Quantum*, 4:321, September 2020.
- [34] Seungchan Seo, Jiheon Seong, and Joonwoo Bae. Mitigation of crosstalk errors in a quantum measurement and its applications. *arXiv preprint arXiv:2112.10651*, 2021.
- [35] Yusong Tan, Fuhui Wu, Qingbo Wu, and Xiangke Liao. Resource stealing: a resource multiplexing method for mix workloads in cloud system. *The Journal of Supercomputing*, 75(1):33–49, 2019.
- [36] Wei Tang, Teague Tomesh, Martin Suchara, Jeffrey Larson, and Margaret Martonosi. Cutqc: using small quantum computers for large quantum circuit evaluations. In *Proceedings of the 26th ACM International conference on architectural support for programming languages and operating systems*, pages 473–486, 2021.
- [37] Swamit S Tannu and Moinuddin K Qureshi. Not all qubits are created equal: A case for variability-aware policies for nisq-era quantum computers. In *Proceedings of the twenty-fourth international conference on architectural support for programming languages and operating systems*, pages 987–999, 2019.
- [38] Runzhou Tao, Hongzheng Zhu, Jason Nieh, Jianan Yao, and Ronghui Gu. Quantum virtual machines. In *19th USENIX Symposium on Operating Systems Design and Implementation (OSDI 25)*, pages 411–428, 2025.
- [39] The Kubernetes. Kubernetes: Production-Grade Container Orchestration. <https://kubernetes.io/>, 2025. Accessed: 2025-12-14.
- [40] Nathaniel Tornow, Emmanouil Giortamis, and Pramod Bhatotia. Scaling quantum computations via gate virtualization. *arXiv preprint arXiv:2406.18410*, 2024.
- [41] Ruixia Wang, Peng Zhao, Yirong Jin, and Haifeng Yu. Control and mitigation of microwave crosstalk effect with superconducting qubits. *Applied Physics Letters*, 121(15), 2022.
- [42] Robert NM Watson, Peter G Neumann, Jonathan Woodruff, Michael Roe, Hesham Almatary, Jonathan Anderson, John Baldwin, David Chisnall, Brooks Davis, Nathaniel Wesley Filardo, et al. Capability hardware enhanced risc instructions: Cheri instruction-set architecture (version 7). Technical report, 2019.
- [43] Mingsheng Ying. *Foundations of quantum programming*. Elsevier, 2024.
- [44] Henry Zou, Matthew Treinish, Kevin Hartman, Alexander Ivrii, and Jake Lishman. Lightsabre: A lightweight and enhanced sabre algorithm. *arXiv preprint arXiv:2409.08368*, 2024.